https://doi.org/10.5194/egusphere-2025-2187
Preprint. Discussion started: 17 June 2025

Quantifying Retrogressive Thaw Slump Mass Wasting and Carbon Mobilisation on the Qinghai-Tibet Plateau Using Multi-Modal Remote Sensing

Kathrin Maier[1], Zhuoxuan Xia[2], Lin Liu[2], Mark J. Lara[3], Jurjen Van der Sluijs[4], Philipp Bernhard[5], and Irena Hajnsek[1,6]

[1]Department of Environmental Engineering, ETH Zurich, 8093 Zurich, Switzerland
[2]Department of Earth and Environmental Sciences, The Chinese University of Hong Kong, Hong Kong, China
[3]Department(s) of Plant Biology and Geography, University of Illinois at Champaign-Urbana, Urbana, IL, USA
[4]Northwest Territories Centre for Geomatics, Government of Northwest Territories, Yellowknife, NWT, X1A 2L9, Canada
[5]Gamma Remote Sensing, Bern, Switzerland
[6]Microwaves and Radar Institute, German Aerospace Centre (DLR), 8053 Wessling, Germany

Correspondence: Kathrin Maier (maierk@ethz.ch)

Abstract. Retrogressive Thaw Slumps (RTS) are slope failures triggered by permafrost thaw, occurring in ground-ice rich regions in the Arctic and on the Qinghai-Tibet Plateau (QTP). A strong warming trend has amplified RTS activity on the QTP in recent years. Although the region currently acts as a carbon sink, its 40 % permafrost-covered area holds substantial soil organic carbon (SOC) stocks. Intensifying thaw-driven mass wasting may transform the QTP into a net carbon source by mobilising previously frozen SOC and increasing decomposition. Despite this, regional remote sensing studies have not yet quantified RTS mass wasting, including material erosion volumes and SOC mobilisation. Analysing time-series data from digital elevation models (DEM) enables direct observation of RTS activity by measuring changes in active area, volume of eroded material, and the overall magnitude of surface change. However, most available DEM sources lack sufficient spatial resolution and temporal frequency for comprehensive RTS monitoring. In contrast, optical data provides higher spatial resolution and more frequent observations, but lacks elevation information. We evaluated the mass wasting of RTS throughout the QTP from 2011 to 2020 by combining DEMs from bistatic Interferometric Synthetic Aperture Radar (InSAR) observations of the TanDEM-X mission with annual RTS inventories derived from high-resolution optical satellite images and geophysical soil property data to estimate erosion volume, ground ice loss, and SOC mobilisation. By combining modelled soil property datasets with multimodal remote sensing data, we estimated that RTS activity in the QTP between 2011 and 2020 relocated $5.02\ ^{25.35}_{0.75} \times 10^7\,\mathrm{m}^3$ formerly frozen material, contributed to $3.58\ ^{28.20}_{0.28} \times 10^6\,\mathrm{m}^3$ loss of ground ice and mobilised $2.78\ ^{7.98}_{0.11} \times 10^8\,\mathrm{kg\,C}$ organic carbon. We found a reliable power law scaling between the RTS area in the optical RTS inventory and the calculated volume change with α = 1.30 $\pm$ 0.01 (R^2 = 0.87, p $<$ 0.001) that potentially allows future research to transform the planimetric RTS area into volume estimates for large-scale and comprehensive investigations on RTS mass wasting and SOC mobilisation in QTP. Despite the comparably recent initiation and smaller size of RTS in QTP, material erosion and SOC mobilisation in the past decade surpassed some regions in the Siberian Arctic but remained up to 10 times lower than hotspots in the Canadian High Arctic. Although the current impact of RTS in QTP is relatively modest, affecting only 0.006 % of the total permafrost area

https://doi.org/10.5194/egusphere-2025-2187
Preprint. Discussion started: 17 June 2025

and contributing less than 1 % to the regional carbon budget, the increasing rates of RTS activity suggest that this phenomenon could become more significant in the future. Our study underscores the importance of regional studies in understanding the impact of permafrost thaw on the carbon dynamics of QTP.

1 Introduction

Permafrost regions are rapidly warming, causing widespread thaw and degradation (Biskaborn et al., 2019; Farquharson et al., 2019; O'Neill et al., 2023). Permafrost thaw is triggered by long-term air temperatures rise (Smith et al., 2022) and is further amplified by various short-term disturbances, such as periods of extreme summer temperatures, high-intensity rainfall, hydrological changes, wildfires, and anthropogenic impacts (Grosse et al., 2011; Hjort et al., 2022; Holloway et al., 2020; Bernhard et al., 2022b; Kokelj et al., 2015). Although approximately half of the global soil organic carbon (SOC) stock is stored in permafrost soils in the northern hemisphere (Mishra et al., 2021; Schuur et al., 2022), ongoing permafrost decline is expected to accelerate SOC decomposition and greenhouse gas emissions, potentially triggering significant climate feedbacks (Schuur et al., 2022; Yi et al., 2025). Due to the lack of large-scale observations and the complexity of the processes, climate models do not account for the potential of permafrost thaw processes when estimating potential permafrost carbon feedbacks (Yi et al., 2025; Schuur et al., 2015, 2022). Existing Earth system models exhibit significant limitations in the accounting of soil organic carbon (SOC) and in the prediction of future changes (Turetsky et al., 2020; Virkkala et al., 2021; Nitzbon et al., 2020).

The Qinghai-Tibet Plateau (QTP) is the largest high-altitude permafrost zone with a total extent of $1.06 \times 10^6\,\mathrm{km}^2$ at mean elevations greater than 4000 m altitude (Wang and French, 1994; Liu and Chen, 2000; Zou et al., 2017). Similarly to high-latitude permafrost regions, QTP stores large amounts of SOC, but exhibits different characteristics from the Arctic, including a thicker active layer, higher ground temperatures, and relatively low ground ice content (Wang et al., 2022). These properties, together with an observed trend of climate warming over the past several decades, make QTP a potential large carbon source and an important region to monitor permafrost thaw processes (Ran et al., 2022; Chen et al., 2024a; Yi et al., 2025). The QTP is susceptible to permafrost thaw processes that cast strong impacts from permafrost degradation, including threats to local transport and energy infrastructure and ecosystems, as well as to regional climate and water storage (Luo et al., 2019; Li et al., 2022; Mu et al., 2017; Zhao et al., 2020; Kokelj and Jorgenson, 2013).

A common, highly visual, and dynamic example of a permafrost thaw process is Retrogressive Thaw Slumping (RTS), defined as a landsliding process in ice-rich permafrost terrain that involves the thawing of ground ice, the collapse of surficial material, and the sliding and flowing downslope of the resulting debris (Nesterova et al., 2024; Harris, 1988; CPA et al., 2024). This mass wasting process leads to the formation of thaw slumps as a thermokarst landform (Burn and Lewkowicz, 1990; Kokelj and Jorgenson, 2013). The landform can expand successively upslope with time due to continuous exposure and thawing of massive and segregated ground ice, thus eroding steep headwalls and mobilising thawed material downslope and potentially into nearby streams and rivers (Nesterova et al., 2024; Kokelj et al., 2021). A gradual decline in headwall height with upslope growth and material accumulation can also result in stabilisation and senescence (Burn and Lewkowicz, 1990; Van Der Sluijs et al., 2023), which can further reactivate again in complex polycyclic ways (see, e.g., Krautblatter et al. (2024);

https://doi.org/10.5194/egusphere-2025-2187
Preprint. Discussion started: 17 June 2025

Tunnicliffe et al. (in preparation)). Climate warming and human disturbance have intensified RTS activity not only in the Arctic (Lantz and Kokelj, 2008; Bernhard et al., 2022a; Van Der Sluijs et al., 2023; Young et al., in review), but also particularly in the QTP, manifesting itself with increased numbers, sizes, and faster retreat rates, especially in the last decade (Xia et al., 2024; Luo et al., 2022; Huang et al., 2021; Yang et al., 2025a). However, due to their complex spatiotemporal dynamics, monitoring RTS activity and assessing its impact on regional carbon cycling remains challenging and is still associated with considerable uncertainties. Most studies have focused on thermokarst hotspots in the central and northeast regions of the QTP, conducting local to subregional analyses using high-resolution satellite imagery and (semi)automatic detection algorithms (Luo et al., 2022; Huang et al., 2021; Xia et al., 2022). A recent study provided an annual inventory of more than 3,000 RTS features across the QTP from 2016 to 2022, using high-resolution optical PlanetScope imagery and a semiautomatic detection approach. This effort represents the first high-quality regional-scale dataset that describes RTS initiation and planimetric expansion in recent years (Xia et al., 2022). Nevertheless, to quantify RTS-induced mass wasting and evaluate the potential implications on permafrost carbon emissions, additional datasets are still required - particularly those capturing lateral and vertical change and soil properties. By deriving elevation change from pairs of high-resolution digital elevation models (DEMs) with a temporal baseline within the affected planimetric RTS boundary, volume changes of the eroded material can be obtained by air- or spaceborne LiDAR, stereo optical photogrammetry or bistatic Interferometric Synthetic Aperture Radar (InSAR) measurements (Lantuit and Pollard, 2005; Van Der Sluijs et al., 2018; Ramage et al., 2018; Dai et al., 2024; Bernhard et al., 2020). Using in-situ measurements or modelled estimates of SOC stocks and ground ice content, we can combine this information with volumetric change estimates to estimate the amount of formerly frozen organic carbon that has been mobilised. Such approaches have been applied to assess carbon mobilisation due to coastal erosion and slumping in Canada (Ramage et al., 2018), a severe heat wave in Siberia (Bernhard et al., 2022b), and more recently at large thaw-driven mass wasting sites across the pan-Arctic (Dai et al., in review). However, to date, there have been no regional-scale estimates of either material erosion volume or SOC mobilisation for the QTP.

In this study, we present the first regional empirical analysis on RTS mass wasting quantifying how much material has been eroded, how much ground ice has been lost and how much SOC has been mobilised due to RTS activity on the QTP during the last decade. Data from the German TanDEM-X mission's X-band bistatic SAR enables the creation of multitemporal DEMs with approximately 10 m spatial resolution and 2 -3 m vertical accuracy (Krieger et al., 2007), suitable for pan-Arctic monitoring of RTS mass wasting (Bernhard et al., 2022b; Maier et al., 2025). Combining the annual high-resolution RTS delineations of Xia et al. (2024) and the elevation change from TanDEM-X-derived DEMs between 2011 and 2020, we estimated the volume change of the eroded material induced by RTS activity on the QTP. Based on recently published datasets on the permafrost state and soil conditions including active layer thickness, volumetric water / ground ice (GI) content, and SOC stocks, we modelled the material erosion volumes into mobilised SOC fluxes for all RTS present on the QTP until 2020 (Ran et al., 2022; Zou et al., 2024; Wang et al., 2021). We evaluated the uncertainty in the estimated erosion volume and the derived properties, examining how spatial resolution affects errors in material erosion estimates. Similarly to temperate landslides, scaling laws between the planimetric area and the erosion volume have been used to improve our understanding of the variability in geomorphology, process dynamics, and the drivers and controls of RTS (Kokelj et al., 2021; Bernhard et al., 2022a; Van Der Sluijs

https://doi.org/10.5194/egusphere-2025-2187
Preprint. Discussion started: 17 June 2025

et al., 2023). By examining the allometric scaling of area and volume of RTS-induced material erosion in QTP we provide a basis for (1) the (sub)regional comparison of RTS dynamics and (2) providing empirical scaling relationships to potentially constrain regional-scale estimates on material erosion and carbon mobilisation. We aim to show that the combination of multi-modal and multitemporal datasets allows for a more detailed analysis of RTS mass wasting dynamics and further increases our understanding of the regional carbon budget impacts.

2 Data and methods

2.1 Study site

Our study region, the Qinghai-Tibet Plateau (QTP), is located between 26° N and 38° N in the south-west of China at average elevations higher than 4000 m above sea level (Fig. 1 a). Permafrost covers 40 % of the plateau (Wang and French, 1994; Liu and Chen, 2000; Zou et al., 2017). The permafrost ground ice content averages around 30 %, decreasing spatially from north to south and west to east, holding a total water volume of 3330 km^3 in the top 10 m (Zou et al., 2024) (Fig. 1 b). Compared to the Arctic, the thickness of the active layer (ALT) is high ($\overline{\mathrm{ALT}}$ = 2.34 m) (Ran et al., 2022), while permafrost thickness is relatively low (<60 - 350 m) (Zhao et al., 2020). A dry and cold climate in the northwest transitions to a warmer and wetter climate in the southeast of the plateau (Chen et al., 2015). The QTP permafrost also stores large amounts of soil organic carbon (SOC) with a median estimate of 1.41 $\times$ 10^{13} $\mathrm{kg\,C}$ (or 14.1 $\mathrm{Pg\,C}$) for the top 3 m and 4.92 $\times$ 10^{13} $\mathrm{kg\,C}$ (or 49.2 $\mathrm{Pg\,C}$) for the upper 25 m of soils (Wang et al., 2020; Chen et al., 2024a). The SOC stocks increase from west to east and from north to south (Wang et al., 2021; Chen et al., 2024a) (Fig. 1 c).

Similar to the Arctic, the QTP is one of the most climate sensitive regions on Earth (Liu and Chen, 2000) and has experienced a pronounced warming trend in recent decades, with an average increase in air temperatures of 0.035° $\mathrm{C\,a^{-1}}$ (Yao et al., 2019). The warming trend affects the thermal state of the permafrost: both ALT and ground temperatures have increased, as the regional permafrost extent declines (Cheng and Wu, 2007; Wu and Zhang, 2008; Zhao et al., 2021; Ran et al., 2022). In addition, the ice-rich terrain in the QTP has become more prone to thermokarst development, likely to affect regional carbon budgets and water storage capacities (Yi et al., 2025; Chen et al., 2024b). In recent years, the Plateau experienced strong expansion and initiation rates of RTS mainly on gentle north-facing slopes with fine-grained soils and high ground ice content. More than 30 % of all RTS activity is observed in a part of the central QTP, namely the Beiluhe River Basin (Luo et al., 2022; Huang et al., 2020; Xia et al., 2022, 2024) (Fig. 1 a). Observations and inventories of RTS activity and historical development are still scarce, but subregional studies focussing mainly on thermokarst hotspots in central QTP indicate that most RTS activity started around 2010 (Luo et al., 2019, 2022; Xia et al., 2024). RTS retreat rates are relatively high, with mean rates up to 25 $\mathrm{m\,a^{-1}}$ (2017 - 2019) (Huang et al., 2021), though similar to other highly active RTS sites in Alaska, northwest Canada, the Canadian High Arctic, and Siberia (Hall et al., in review).

https://doi.org/10.5194/egusphere-2025-2187
Preprint. Discussion started: 17 June 2025

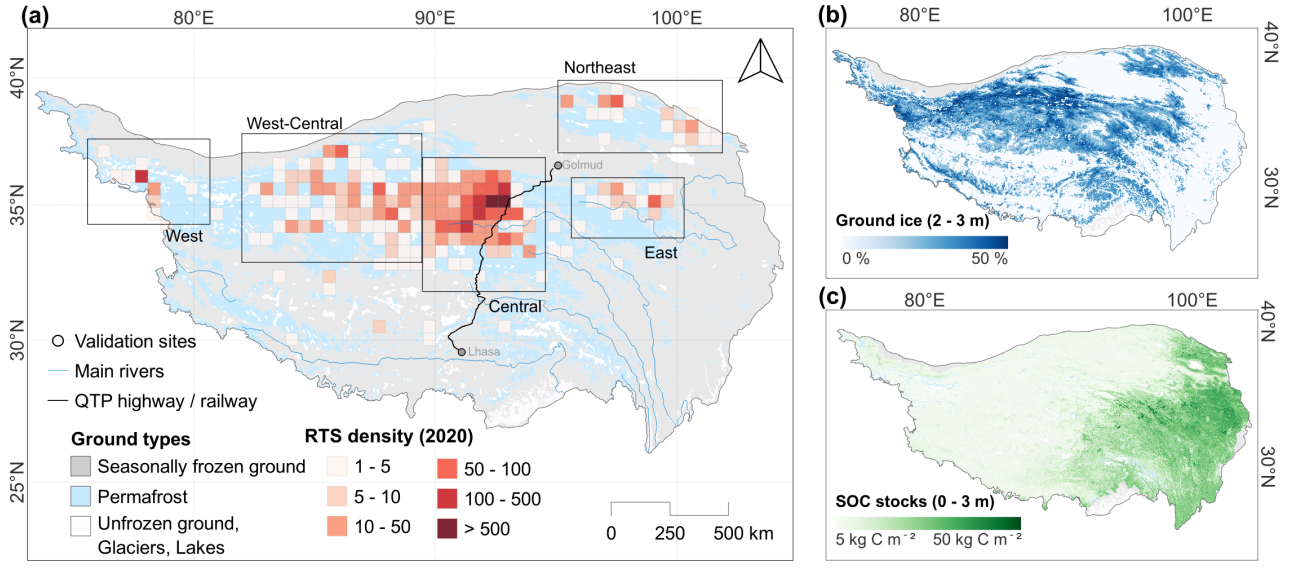

Figure 1. **(a)** Distribution of RTS on the Qinghai-Tibet Plateau (QTP) Xia et al. (2024). We divided the QTP into five subregions (West, West-Central, Central, East, Northeast) based on spatial RTS clusters (Xia et al., 2024) and distributed validation sites (400 km^2) across the QTP. Distribution of permafrost and seasonally frozen ground on the QTP from Zou et al. (2017). **(b)** Volumetric ground ice content between 2 and 3 m depth modelled with a random forest algorithm based on climate, terrain and soil variables and $>$ 600 borehole records (Zou et al., 2024). **(c)** Soil organic carbon (SOC) stocks aggregated for the first 3 m depth derived with a set of machine learning algorithms together with environmental variables and soil profile data from $>$ 500 field measurements (Wang et al., 2021) show an increasing trend from northwest to southeast QTP.

2.2 Workflow and data processing

Based on the spatial clustering of RTS identified by Xia et al. (2024), we divided the study area into five subregions, which include the West, West-Central, Central, Northeast and East (Fig. 1) to analyse spatial patterns of material erosion and mobilisation of SOC induced by RTS activity in the QTP. To validate the estimated volumes of RTS material erosion derived from integrated optical and elevation remote sensing data, we established several validation sites that were spatially distributed throughout the QTP.

We used bistatic TanDEM-X SAR observations to generate multi-temporal DEMs that span all RTS locations in the RTS inventory of Xia et al. (2024). The elevation change between 2011 and 2020 was retrieved by a series of processing steps (e.g., Fig. 2 a). The active erosion area δ A was estimated after Xia et al. (2024), where high resolution multispectral satellite imagery was used to detect and delineate RTS boundaries (Fig. 2 b). These areas, in combination with soil property datasets for the QTP, allowed us to estimate the volume of eroded material, associated ground ice loss, and mobilisation of SOC (Fig. 2 c).

https://doi.org/10.5194/egusphere-2025-2187
Preprint. Discussion started: 17 June 2025

We validated our approach (1) by manually delineating actively eroded sections of the RTS from elevation change products and comparing their spatial overlap with optically derived RTS delineations; and (2) by comparing maximum elevation changes from TanDEM-X DEMs with average headwall heights derived from very high-resolution (VHR) DEMs from 6 RTS in the Beiluhe River Basin in Central QTP, obtained from drone photogrammetric surveys conducted in the summer of 2020 (Fig. 2 d).

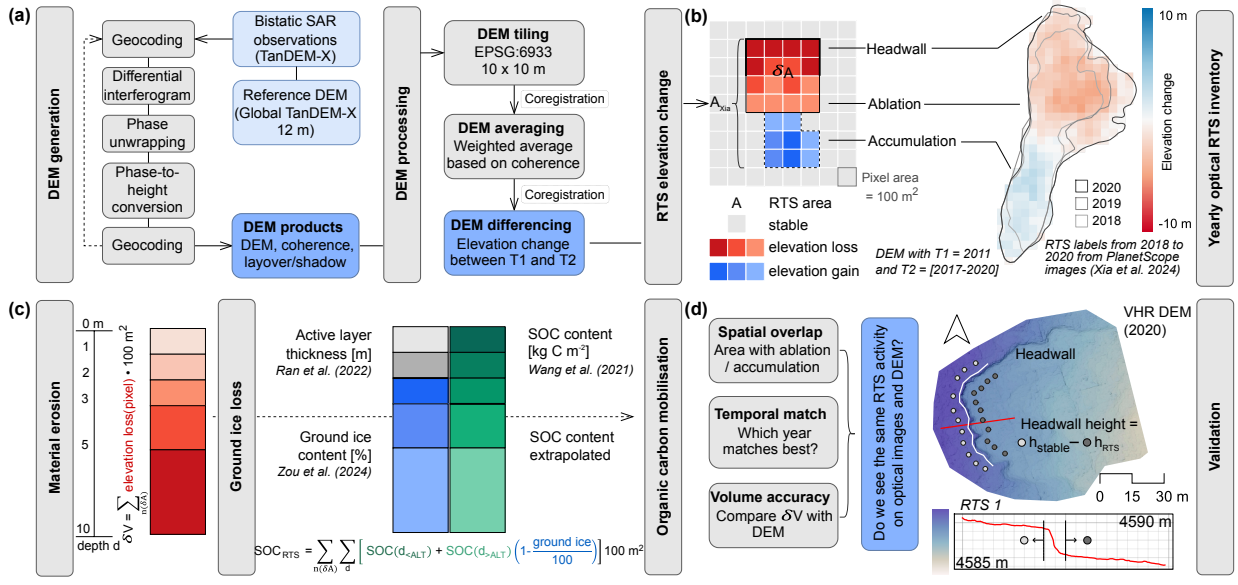

Figure 2. Data processing and validation: **(a)** DEM generation from TanDEM-X SAR observations based on bistatic interferometric SAR (InSAR) processing and post-processing with data tiling, averaging, and differencing including coregistration routines resulting in elevation change maps between time T1 and T2. **(b)** We extract the elevation change (T2-T1) within the boundaries of the temporally matching optical RTS labels of Xia et al. (2024) divided into negative elevation change (ablation) and positive elevation change (deposition of thawed material) within the RTS delineation. **(c)** Estimation of the properties of RTS mass wasting including material erosion calculated from negative elevation change within the RTS boundary, ground ice (GI) loss based on ground ice content from Zou et al. (2024) and the ALT dataset from Ran et al. (2022), and SOC mobilisation incorporating SOC stocks from Wang et al. (2021) and an extrapolation approach adapted from Bernhard et al. (2022b) and Ramage et al. (2018). **(d)** Validation at selected sites by (1) evaluating how accurately we can estimate δ A and δ V based on the optical labels and (2) by comparing headwall heights obtained from VHR DEMs of six RTS in the Beiluhe River Basin from photogrammetric drone surveys in 2020 to our results.

2.2.1 Digital Elevation Model generation and processing

The German Synthetic Aperture Radar (SAR) satellite mission TanDEM-X allows us to generate temporally resolved digital elevation models based on bistatic SAR interferometry (InSAR) (Krieger et al., 2007; Bojarski et al., 2021). We excluded observations with height-of-ambiguity (HoA) values below 15 and above 80 m to guarantee a vertical accuracy between 2 and

https://doi.org/10.5194/egusphere-2025-2187
Preprint. Discussion started: 17 June 2025

3 m in flat areas (Martone et al., 2012; Bernhard et al., 2020). Bernhard et al. (2020) found in Arctic thermokarst landscapes that observations during summer can challenge RTS monitoring due to increased elevation uncertainties and errors attributed to late winter snow, as well as dense and wet tundra vegetation that changes the dielectric properties of signals. Therefore, studies relying on SAR-based DEMs for RTS monitoring typically use only winter observations (Bernhard et al., 2022a; Maier et al., 2025), where the assumption is that X-band radar waves penetrate dry snowpacks up to several metres (Leinss and Bernhard, 2021; Millan et al., 2015). However, in the QTP, we can only achieve full spatial coverage if we use year-round observations. Compared to Arctic permafrost regions, the QTP is characterised by different climate and vegetation that mitigates some problems. For example, the maximum accumulation of snow on the QTP between December and February has a low mean snow depth of < 1 to 11 cm (< 1 cm standard deviation (SD)) and a maximum accumulation of < 2 m (Che et al., 2008; Yang et al., 2020) which is well below the height sensitivity of TanDEM-X DEM. The central QTP, where most RTS are located, has the lowest average snow depth observed in recent decades on the Plateau (Ma et al., 2023). In addition, the vegetation characteristics support our approach of incorporating year-round TanDEM-X observations for DEM generation. The vegetation in which most RTS are located is characterised by low canopy heights, such as alpine meadows and steppes, arid desert, or even bare ground (Wang et al., 2016; Xia et al., 2024).

Using the global 12 m spatial resolution TanDEM-X DEM as a reference, pairs of bistatic SAR observations were processed with the GAMMA Remote Sensing software (Werner et al., 2000) following a standard InSAR processing workflow, to generate a series of DEM products (Fig. 2 a). SAR shadow and layover areas, as well as the regions in the SAR images that experienced low coherence (< 0.3), were not considered in subsequent processing (Bernhard et al., 2020; Maier et al., 2025). Based on the interferometric coherence, the observation's HoA and the multilooking window (4×4 pixels), we estimated the associated random elevation error σ_h of each pixel for all generated DEMs (Krieger et al., 2007; Rosen et al., 2000; Rodriguez and Martin, 1992). Following Maier et al. (2025), we reprojected all DEM products to a common horizontal coordinate system, WGS 84 / NSIDC EASE-Grid 2.0 Global (EPSG:6933) with ellipsoidal vertical reference, resampled to 10 m spatial resolution and split all data into 100 km^2 tiles with a small spatial overlap to avoid edge effects. We corrected the DEMs for vertical offsets and tilts and co-registered the DEM pairs using the Python package xDEM (Hugonnet et al., 2021). Due to the non-uniform temporal coverage of TanDEM-X observations in the QTP, we decided to calculate the elevation change δh between two time periods. We averaged all available DEMs for the time period T1 that spans one summer period (01/2011 - 04/2012) and for T2 that spans two summer seasons (09/2017 - 01/2020). In case of the existence of several DEMs in the same location during the same time period, we calculated a weighted average per pixel based on interferometric coherence before computing the elevation difference T2 - T1 for each tile with RTS activity based on the RTS inventory of Xia et al. (2024). The resulting elevation change maps are normally distributed around zero with a SD representing the achievable vertical accuracy of the DEM pair. $\delta h \sim 0$ m indicates stable terrain, while negative and positive values reflect material ablation and deposition of thawed materials, respectively.

https://doi.org/10.5194/egusphere-2025-2187
Preprint. Discussion started: 17 June 2025

2.2.2 Multimodal RTS mass wasting quantification

Xia et al. (2024) created a high-quality regional inventory of annual RTS delineations between 2016 and 2022 based on a semi-automated deep learning approach with high-resolution PlanetScope imagery (Xia et al., 2022) (Fig. 2 b). The DEMs of T2 consist of up to two summer seasons of RTS activity, depending on the availability and spatial distribution of the observations. If the data from T2 consisted only of observations from one year, the optical RTS label from the matching year was selected as RTS delineation for mass wasting calculations. If observations from several years contributed to the DEM of T2, we assigned the optical RTS shape that matched the last observation year to ensure a conservative estimation of the eroded volume. Spectral information in optical images distinguishes undisturbed from disturbed terrain, using differences in vegetation cover. RTS delineations derived from optical imagery often encompass a broader area than the active ablation zone, including zones of recent activity and depositional sections of the slump floor (i.e., features not directly involved in ongoing material loss), while excluding stable zones of past disturbance masked by lush vegetation growth. Therefore, we calculated the volume of eroded material δV for each RTS by summing only the negative elevation changes $\delta h_{<0\ m}$ multiplied by the area of the DEM pixel (Fig. 2 c).

$$\delta V = \sum \delta\, h_{<0\ m} \cdot 100\ \mathrm{m}^2 \tag{1}$$

Adapted from temperate landslide research, we applied a relationship between area and material erosion volume, the so-called area-volume or allometric scaling, to investigate RTS properties and to be able to compare morphological enlargement characteristics with other studies (Jaboyedoff et al., 2020; Kokelj et al., 2021; Bernhard et al., 2022a; Van Der Sluijs et al., 2023). Following the methodology of Bernhard et al. (2022a), we use an orthogonal distance regression model to fit a straight line in log space (Boggs and Rogers, 1989) and predict the eroded volume δV based on the planimetric area δA with an exponential scaling coefficient α and a scaling factor c (Jaboyedoff et al., 2020) for the time interval T1 - T2.

$$\delta V = c \cdot \delta A^{\alpha} \tag{2}$$

Notably, δA stands for the RTS area that undergoes a negative elevation change or ablation and, therefore, is actively eroding within the monitoring period of T1-T2. Instead, the RTS delineations of Xia et al. (2024) based on optical imagery distinguished between disturbed zones and intact vegetation. To test the influence of slightly different definitions of the RTS area, we also performed area-volume scaling with the entire RTS delineation area A_{Xia}, which does not include purely active erosion, but also bare soils disturbed by mud flows and the deposition of thawed material in the slump floor (Fig. 2 b).

To estimate how much SOC is stored in the previously frozen permafrost soils mobilised by RTS activity during the study period, ground conditions must be known or modelled (Fig. 2 c). Therefore, we integrate existing datasets for QTP that define (1) ALT, (2) GI content between 2 and 10 m, and (3) SOC stocks between 0 and 3 m depth. All datasets are sampled in 1 km^2 cells. (1) Ran et al. (2022) estimated permafrost thermal state variables including ALT for the pan-Arctic permafrost region and QTP with 452 field measurements with statistical learning models that achieve a root mean square error (RMSE) < 1 m. (2) Zou et al. (2024) estimated the volumetric water / ground ice content up to 10 m depth with a random forest algorithm based on climate, terrain and soil variables and 664 borehole records with $R^2 > 0.8$ for all depth layers (Fig. 1 b). (3) Wang et al.

https://doi.org/10.5194/egusphere-2025-2187
Preprint. Discussion started: 17 June 2025

(2021) applied a set of machine learning algorithms together with environmental variables and soil profile data from 572 field measurements to predict the spatial distribution of SOC in the upper 3 m, including an uncertainty layer in the QTP. The model achieved R^2 values between 0.66 for the upper 30 cm and 0.54 for the first metre (Fig. 1 c). Since the SOC stocks dataset is limited to the upper 3 m, we apply an exponential decay model to extrapolate the values to lower depths where we propagate the uncertainty estimates of 2 - 3 m (Bernhard et al., 2022b). Based on the assumptions that (1) ground ice starts at the depth where the active layer ends and (2) SOC is not present in any form in the massive ground ice, we sampled the negative elevation change within each RTS label to calculate the SOC mobilisation per RTS

$$\mathrm{SOC_{RTS}} = \sum_{n(\delta A)} \sum_{d} [\mathrm{SOC(d_{<ALT})} + \mathrm{SOC(d_{>ALT})}(1 - \frac{\mathrm{GI}}{100})]\ 100\ \mathrm{m^2} \tag{3}$$

with the number of pixels n, the RTS ablation area δA and soil depth d. If the depth d is lower than the ALT, then only the part of the eroded material that is not massive ground ice is added to the total SOC mobilisation. Similarly, we estimate the volume of RTS-induced ground ice loss across the depth layers by multiplying the eroded material by $1 - \frac{\mathrm{GI}}{100}$.

We report the total estimates of the volume of eroded material, the mobilisation of SOC, and the loss of ground ice as the sum over all RTS in the study region and throughout the study period. By dividing SOC mobilisation by the number of years between T1 and T2, we estimate SOC fluxes per year. However, the values might be partially biased since we cannot distinguish between RTS that have been active for the entire study period and those that may have only been active for a shorter period of time (Bernhard et al., 2022b). We normalise our results by study area and number of RTS to ensure comparability.

2.2.3 RTS material erosion error assessment and validation

Since we aim to integrate two datasets with distinctly different spatial resolutions (DEM: 10 m, optical RTS inventory: 3 m), we have to account for the ambiguity produced. Negative elevation change pixels might only partially intersect the RTS delineation instead of being entirely contained. We chose to rasterise the optical RTS delineations into two parts: an upper-bound RTS area δA_+ that includes all intersected pixels, and a lower-bound area δA_- with only fully contained pixels. Together with the estimated elevation error σ_h of the DEM we then compute the upper and lower volume limits $\delta V_{+/-}$ that indicate the uncertainty induced by differences in spatial resolution, boundary mismatch, and vertical DEM error.

$$\delta V^+ = \sum_{n(\delta A^+)} (\delta h_{<0m} - \sigma_h) \cdot 100\ \mathrm{m^2} \tag{4}$$

$$\delta V^- = \sum_{n(\delta A^-)} (\delta h_{<0m} + \sigma_h) \cdot 100\ \mathrm{m^2} \tag{5}$$

Together with the uncertainty estimates of the SOC stocks, we propagate the error bounds to all reported quantities. The lower spatial resolution of the DEMs derived from TanDEM-X together with a typical height sensitivity of approximately 2 to

https://doi.org/10.5194/egusphere-2025-2187
Preprint. Discussion started: 17 June 2025

3 m on flat terrain (Krieger et al., 2007) could create discrepancies since the size and depth of small RTS approach monitoring limitations. If an RTS that is present in the optical RTS inventory is smaller or shallower than a certain threshold related to the spatial resolution and vertical sensitivity of the DEM, the resulting elevation change would not show any distinguishable difference from the DEM background noise. Moreover, manually delineating the RTS boundaries depends on the level of expertise and (field-based) familiarity, as well as the data source and ontological definitions (Maier et al., 2025; Van Der Sluijs et al., 2023; Nitze et al., 2024b). In optical imagery, annotators use a snapshot in time and distinguish disturbed ground from intact vegetation to define the boundaries of an RTS; on elevation change maps, we identify the cumulative RTS activity over time by the regions that show ablation (= negative elevation change).

To understand the impact of these potential drawbacks on our proposed multimodal RTS monitoring method, we performed a two-fold validation at five sites spread over the QTP (Fig. 1 a). First, we manually delineated the RTS ablation in the elevation change maps, where a distinct pattern of negative elevation change is visible to the human eye. All elevation change maps consist of DEMs from 2011 and 2019. We statistically compared the RTS labels from the optical inventory of Xia et al. (2024) from the same year (2019), the year before (2018) and the year after (2020) to the DEM-based delineations in terms of absolute numbers, area, and derived material erosion volume (Fig. 2 d). Furthermore, we performed a comparison between TanDEM-X-derived DEMs and very high resolution (VHR) photogrammetric DEMs from in situ drone campaigns of a total coverage of 68520 m^2 in August 2020. We used a DJI P4 Multispectral to obtain the multispectral drone images. The resulting DEM has a spatial resolution of < 1 m and a georeferencing accuracy of 0.2 m RMSE. Since no VHR DEM was available for T1, we could not perform DEM differencing and directly validate our volume change estimates. Furthermore, only data from six RTS in the central cluster were available for independent validation. Based on the VHR DEM and its hillshade version, we manually delineated the approximate location of the headwall with the help of transect profiles. We defined small buffer zones (~ 5 m) and randomly distributed points (n = 100 per RTS) on both sides of the headwalls that represent the elevation of stable ground $\mathrm{h}_{\mathrm{stable}}$ and the RTS slump floor $\mathrm{h}_{\mathrm{RTS}}$, respectively. We computed the average headwall height $\overline{\mathrm{h}_{\mathrm{VHR}}}$ per RTS as the difference median of $\mathrm{h}_{\mathrm{stable}}$ and $\mathrm{h}_{\mathrm{RTS}}$ (Fig. 2 d). We compare the VHR headwall heights with the maximum negative elevation change $\delta h_{\max}$ that we estimated based on TanDEM-X DEMs.

3 Results

After we present regional estimates of RTS-induced material erosion and carbon mobilisation, and the spatial distribution within QTP, we provide a detailed analysis of the heterogeneity of RTS activity on subregional scale. We report the results of the area-volume scaling performed between the RTS area and the erosion volume and investigate the accuracy of the proposed method with independent data at several test sites distributed throughout the region.

https://doi.org/10.5194/egusphere-2025-2187
Preprint. Discussion started: 17 June 2025

3.1 RTS mass wasting on the QTP between 2011 and 2020

Out of 3,613 RTS delineations of Xia et al. (2024) that we matched with the generated elevation change maps, we excluded 2 % (71 RTS) from further analysis due to low SAR coherence or SAR layover / shadow regions. For these discarded RTS, reliable erosion volume estimates are not possible due to low confidence in DEM quality.

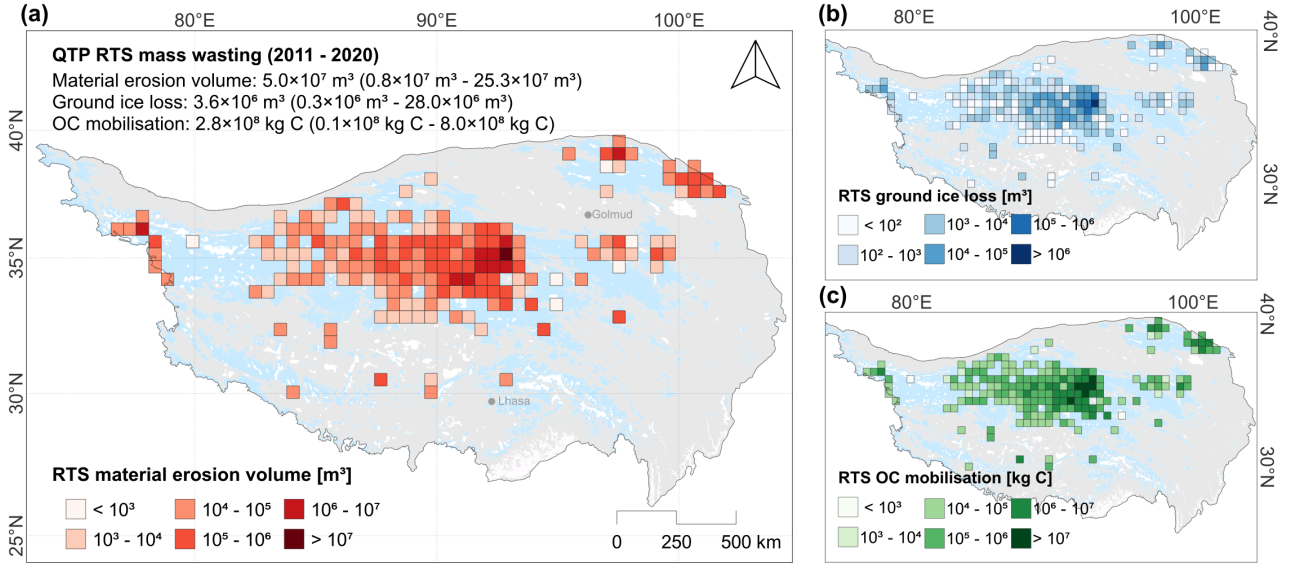

Figure 3. Total RTS mass wasting in the QTP between 2011-2020: RTS mass wasting activity is the highest in central QTP. **(a)** Material erosion volume from RTS activity. **(b)** Total GI loss from RTS activity. **(c)** Total SOC mobilisation from RTS activity. All data are aggregated in 50-km-grids for visualisation purposes.

We estimated a total volume of eroded material δV between 2011 and 2020 induced by RTS activity in QTP of $5.02\ ^{25.35}_{0.75} \times 10^7\ \mathrm{m}^3$ (Fig. 3a). Approximately 50 % of the volume change originates from 0 -1 m, 28 % from 1 - 2 m, and 13 % from 2 - 3 m depth. On average, 65 % of the delineated RTS areas from the optical inventory of Xia et al. (2024) have actively eroded between 2011 and 2020. The median active erosion area δA per RTS was 5200 m^2 compared to the entire optical RTS delineation area $\mathrm{A_{Xia}}$ (including the accumulation and inactive parts of an RTS) of 8000 m^2. We estimated a median volume loss of $6534 \pm 2284\ \mathrm{m}^3$ corresponding to a relative error in elevation change of $\sim 35\%$. The median elevation loss that roughly indicates the RTS headwall height was 1.2 ± 0.4 m. When fitting a linear model to the log-transformed area δA and material erosion volume δV, we found a power law relationship for the area-volume scaling of RTS on the QTP of

$$\delta V = 0.09 \cdot \delta A^{1.30 \pm 0.01} \tag{6}$$

with R^2 = 0.87 ($p<0.001$, Fig. S1 a). We obtain the same scaling coefficient to predict volume change based on the entire area of the RTS delineations $\mathrm{A_{Xia}}$ (Fig. S3 a). However, the fit is slightly noisier and manifests itself in a lower confidence

https://doi.org/10.5194/egusphere-2025-2187
Preprint. Discussion started: 17 June 2025

(R^2 = 0.75). An α value of 1.30 indicates that RTS in QTP during the last decade followed a relationship between linear growth (α = 1.0) and exponential growth (α > 1.5) and falls in the range of soil landslides (1.1 - 1.4) based on the investigated scaling relations of landslides in temperate locations (Jaboyedoff et al., 2020).

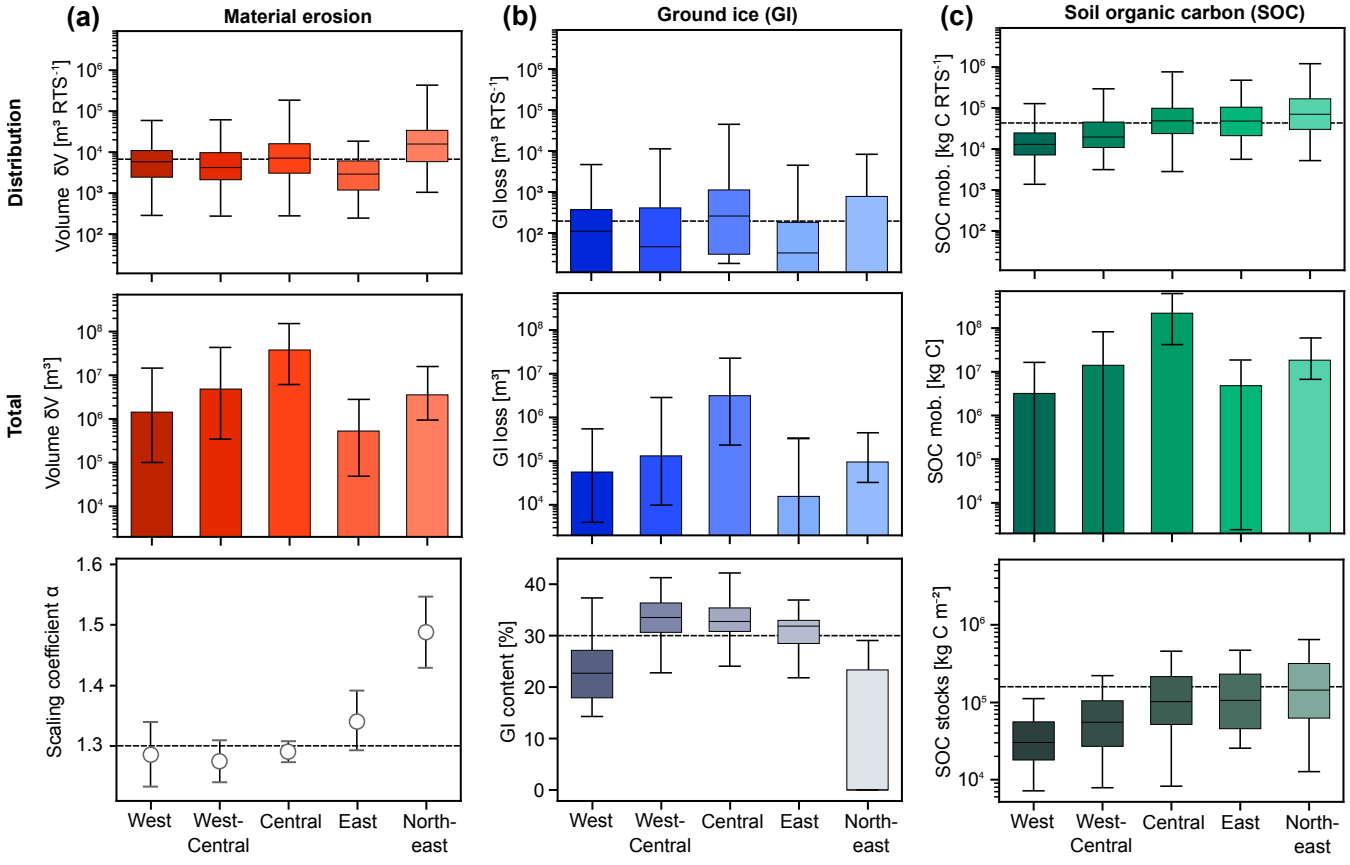

Figure 4. RTS mass wasting quantities between 2011 and 2020 in QTP subregions: First row displays a box plot of the quantity's distribution per RTS, the second row the total quantity per subregion, and the third row additional data. **(a)** RTS material erosion and area-volume scaling coefficients for the subregions with R^2 between 0.77 ($p<0.001$, West) and 0.89 ($p<0.001$, Central). **(b)** RTS ground ice loss and the distribution of GI content (Zou et al., 2024). **(c)** RTS induced SOC mobilisation and the distribution of SOC stocks 0 - 3 m (Wang et al., 2021). Number of RTS n_{RTS} per subregion: West = 170, West-Central = 523, Central = 2688, East = 76, Northeast = 140.

The median GI content at the RTS locations extracted from Zou et al. (2024) was 31 %. We also estimated that $3.58^{28.20}_{0.28}$ $\times$ 10^6 m^3 massive ground ice has been lost during the last decade (Fig. 3 b). We calculated that $\sim$ 64 % of the thawed ground ice was located in the first metre under the active layer (2 - 3 m), 32 % between 3 and 5 m and the remaining 4 % below 5 m depth. Based on data on SOC stocks of Wang et al. (2021), we calculated a total SOC mobilisation from RTS erosion of $2.78^{7.98}_{0.11}$ $\times$ 10^8 kg C (Fig. 3 c). We found annual RTS-induced SOC fluxes of 0.35 $\times$ 10^8 kg C a^{-1}. The first metre of soil contributed $\sim$ 76 %, the second $\sim$ 14 %, and the third $\sim$ 8 % to the total SOC mobilisation.

https://doi.org/10.5194/egusphere-2025-2187
Preprint. Discussion started: 17 June 2025

Xia et al. (2024) found the highest number of RTS (∼ 75 %) in the central Plateau, including the highest area expansion rates. Figure 4 displays a similar pattern of 78 % material erosion volume, 89 % ground ice loss and 81 % SOC mobilisation attributed to the Central QTP. We normalised the total quantities per subregion by RTS count and analysed the distributions to ensure better comparability. We found that even though the central Plateau exhibited the highest absolute amounts due to the highest density of RTS, the volume distribution per RTS was highest in the northeast QTP (Fig. 4 a). The scaling coefficients range from α = 1.27 - 1.29 (R^2 = 0.77 - 0.89, p<0.001) in the West, West-Central and Central subregions to α = 1.47 $\pm$ 0.05 (R^2 = 0.87, p<0.001) in Northeast QTP. This points to a greater elastic distortion in the degree to which the concavity increases volumetrically with changing area for the mountainous northeast QTP (see Van Der Sluijs et al. (2023) for coefficient interpretation, Fig. S1 and Fig. S3). Based on Zou et al. (2024), the GI content is highest in the central subregions (median of 32.8 % in central and 32.6 % in west-central QTP) and lowest in the northeast (median of 0 %, mean of 10.7 %). We found the highest total and per-RTS loss in ground ice in the central subregion, but the total amount is relatively low for the entire QTP compared to the eroded volume (Fig. 4 b). The total amount of SOC mobilised from RTS activity for the QTP subregions shows a pattern similar to material erosion and ground ice loss: Central QTP dominates all RTS mass wasting quantities through the largest number of RTS present. However, the distribution of SOC mobilisation follows the spatial trend present in the SOC stocks from Wang et al. (2021) and the average SOC mobilisation per RTS increases from the west to the northeast of the QTP (Fig. 4 c). Details can be found in the Supplement (Table S1 and S2).

3.2 Assessment of InSAR DEM- and optical-based monitoring of RTS mass wasting in the QTP

We manually delineated the ablation zones for 307 RTS scars on elevation change maps (2011 - 2019) at all validation sites and statistically analysed the potential differences from the RTS labels (2018, 2019, 2020) in the optical inventory of Xia et al. (2022). For the optical RTS labels from 2019 (n = 445), we found an overall good agreement for the total number of RTS found in both datasets with an F1 score of 0.63. 290 RTS were present in both datasets, 17 could only be detected in the DEMs, whereas 155 RTS were not distinguishable from background noise in the elevation change maps and only present in the optical inventory. Most of the validation sites showed good agreement (Fig. 5 a) except for the site in western QTP where only 55 % of the RTS were visible in both datasets. More details on individual results at the test sites can be found in the Supplement (Table S3). Figure 5 b shows an example RTS in the Beiluhe River Basin in Central QTP including the delineations of the optical inventory (Xia et al., 2022) of the summers one year before, the same year and one year after the SAR observation used for the DEM generation, as well as the manually delineated ablation zone visible on the elevation change map.

A RTS delineation based on multispectral imagery defines the boundary of the thaw feature by the difference in the spectral signal between disturbed and intact vegetation, whereas elevation maps showcase RTS activity by elevation loss (ablation at the headwall) and gain (accumulation at the floor). Typically, a larger planimetric area is present in RTS delineations based on optical images that often comprise most of the recently active slump floor and accumulation zone compared to the DEM-based boundaries. However, the overlap at the headwall between the two delineations is adequate, and most of the ablation is part of the optical label. Due to the lower spatial resolution of the DEM, the differences between the optical delineations of 2018, 2019, and 2020 are rather small in this example (Fig 5 b). Comparing the RTS delineation area A_{Xia} with the active erosion

https://doi.org/10.5194/egusphere-2025-2187
Preprint. Discussion started: 17 June 2025

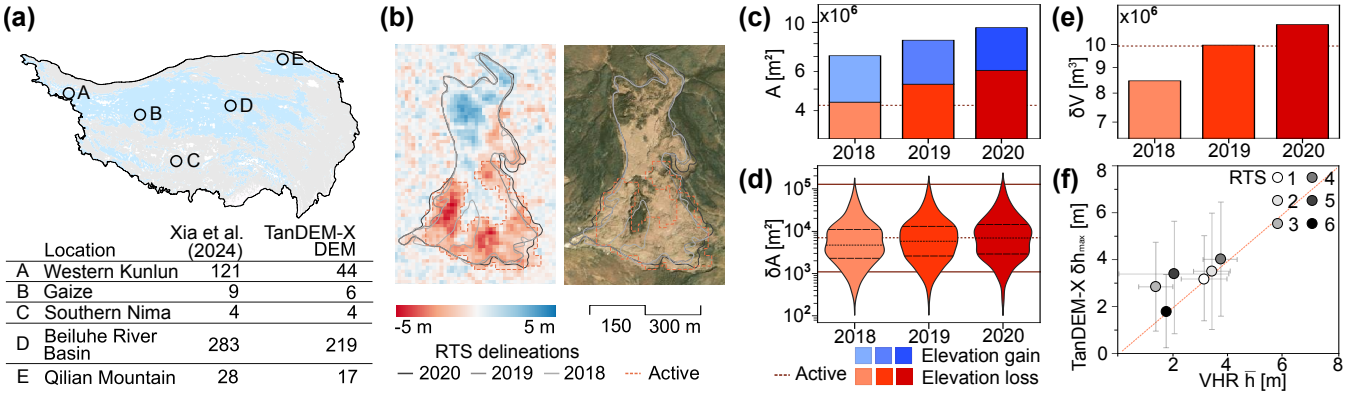

	Location	Xia et al. (2024)	TanDEM-X DEM
A	Western Kunlun	121	44
B	Gaize	9	6
C	Southern Nima	4	4
D	Beiluhe River Basin	283	219
E	Qilian Mountain	28	17

Figure 5. Assessing compatibility and accuracy of multimodal remote sensing for RTS monitoring in the QTP: **(a)** Map of validation sites across the QTP. Number of RTS present in the optical RTS inventory (Xia et al., 2024) per site and number of the same RTS also detectable in the elevation change maps (DEM). **(b)** Example of an RTS in the Beiluhe River Basin with the RTS labels between 2018 and 2020 from Xia et al. (2024) and the manually delineated ablation zone on the elevation data on an TanDEM-X derived elevation change map (DEM_{2019} - DEM_{2011}) and on ESRI satellite base layer (2025). **(c)** Area: Comparing the total ablation and accumulation area based on the elevation loss / gain pixels for the RTS delineations (2018 - 2020) shows that the optical RTS delineations tend to cover a larger area than actual ablation area distinguishable on the DEM (red-dotted line). **(d)** The distribution of the RTS ablation area from 2019 is the closest to the actual mean ablation area. Due to the lower resolution of DEMs, small RTS cannot be captured compared to the optical RTS inventory. Red dotted and solid lines indicate the mean, minimum / maximum values, respectively, based on DEM-annotated active RTS ablation area. **(e)** Material erosion volume: Total material erosion volume calculated based on the RTS ablation area from 2019 shows the best match to actual active ablation area while estimates based on the labels from 2018 under- and from 2020 overestimate the volume change, respectively. **(f)** We compare average headwall height of 6 RTS in the Beiluhe River Basin (Central QTP) from VHR DEM (2020) to the maximum elevation loss δh_{max} of the TanDEM-X DEM and the 2019 optical RTS delineation.

area visible on the elevation change map, we see that the delineations for 2019 and 2020 include substantially more ablation area than what is distinguishable as RTS-induced erosion on the elevation change maps (Fig. 5 b, c). The distribution of the ablation area of the optical RTS labels is rather similar despite the difference in observation time (Fig 5 d). The median actively eroded area per RTS in the validation sample based on manual delineations in the elevation change maps is 12,978 m^2, which is relatively close to the optical RTS labels: 9,748 m^2 in 2018, 11,325 m^2 in 2019, and 13,512 m^2 in 2020 accounting for 62 to 64 % of the total optical delineation area. The lower threshold for distinguishing an RTS from background noise is substantially higher in the elevation change maps based on 10-m-resolution TanDEM-X DEMs (red solid line in Fig 5 d, 1100 m^2) than in the 3-m-resolution PlanetScope images (Xia et al., 2022). In our analysis of the entire QTP, only 6 % of 3613 RTS have ablation areas below this threshold.

The total volume of material erosion (based on the ablation area) diverges in both directions for the delineations of different years (Fig. 5 e). We estimated a total volume δV based on the ablation area covered by optical labels of 8.47, 9.98, and $10.97 \times 10^6\ \mathrm{m}^3$ for 2018, 2019, and 2020, respectively. Compared to the actual total volume based on the manual delineation

https://doi.org/10.5194/egusphere-2025-2187
Preprint. Discussion started: 17 June 2025

of the ablation areas in the elevation change maps of $9.94 \times 10^7\ \mathrm{m}^3$, the optical label of 2019 shows the best fit. The uncertainty of volume change is greater for optical RTS labels compared to the validation (Table S3). For all regions that did not undergo any erosion in the RTS scar or in the vicinity, we assume that the elevation change is normally distributed around zero with a standard deviation of approximately 2 - 3 m in flat terrain for TanDEM-X-derived DEMs. For volume estimation based on optical delineations, stable areas containing noise are likely included since most optical RTS boundaries are larger than the actual active erosion area. Although this minimally affects the total volume change estimate due to the low magnitude in negative elevation change, it adds additional random errors, thus contributing to the overall uncertainty budget.

To further validate our results, we used very high-resolution (VHR) DEMs generated on the basis of drone stereo photogrammetry from August 2020. Fig. 5 f shows a reasonable fit between the maximum elevation changes within the 6 RTS based on the combination of TanDEM-X derived DEMs and optical RTS delineations and the average headwall height calculated from the VHR DEM. Details can be found in the Supplement in Table S4. However, the small sample size does not allow meaningful statistical analysis and, therefore, only allows for a qualitative comparison.

4 Discussion

4.1 Comparing RTS activity and material erosion in QTP to Arctic thermokarst regions

We present the first regional study that estimates the volume of material erosion, ground ice loss, and SOC mobilisation from RTS activity in the QTP over the last decade to improve our knowledge of the characterisation of RTS mass wasting and its influence on the permafrost carbon cycle. Some site-specific and regional studies have investigated the volume of RTS material erosion (Lantuit and Pollard, 2005; Kokelj et al., 2015; Günther et al., 2015) and the allometric scaling relations for thaw-driven mass wasting (Kokelj et al., 2021; Van Der Sluijs et al., 2023), most of them for regions $<$ 10,000 km^2. Instead, Bernhard et al. (2022a) estimated annual material erosion rates for ten regions spread throughout the Pan-Arctic permafrost region in Canada, Alaska, and Siberia with a total study area of 220,000 km^2 using DEMs derived from TanDEM-X observations, while Dai et al. (in review) used ArcticDEM time series to assess volumetrics, scaling relationships, and SOC mobilisation for large thaw-driven mass wasting sites across the Arctic, but not QTP. In QTP, we found RTS material erosion rates of $6.36^{32.1}_{0.95} \times 10^6\ \mathrm{m}^3\ \mathrm{a}^{-1}$. Bernhard et al. (2022a) estimated erosion rates between $< 0.5 \times 10^6\ \mathrm{m}^3\ \mathrm{a}^{-1}$ in Alaska (Fig. 6, location A) and the Siberian Arctic (F - H) and $7.16 \times 10^6\ \mathrm{m}^3\ \mathrm{a}^{-1}$ in the Canadian Arctic (A - D) between 2010 and 2017. With 5.2 RTS per 100 km^2 between 2010 and 2020, QTP has an RTS density approximately half of what Bernhard et al. (2022a) observed between 2010 and 2017 on Banks Island (location B), however, more than double that of all other Arctic sites investigated. Normalised by study area, the RTS in QTP relocated 101.8 $\mathrm{m}^3\ \mathrm{a}^{-1}\ \mathrm{km}^2$ material during the last decade, which is more than 4, 6, and 10 times less than the Canadian hotspots for hillslope RTS (Lewkowicz and Way, 2019) on Peel Plateau (D), Ellesmere Island (A), and Banks Island (B), respectively (Fig 6 b). All remaining sites investigated by Bernhard et al. (2022a) in the Canadian (C), Alaskan (E), and Siberian (F - H) Arctic showed less than half the magnitude of the volume change rates observed in the QTP. Most of these sites are mainly characterised by smaller and shallower RTS located on lake shores in relatively flat terrain (Nesterova et al., 2020).

https://doi.org/10.5194/egusphere-2025-2187
Preprint. Discussion started: 17 June 2025

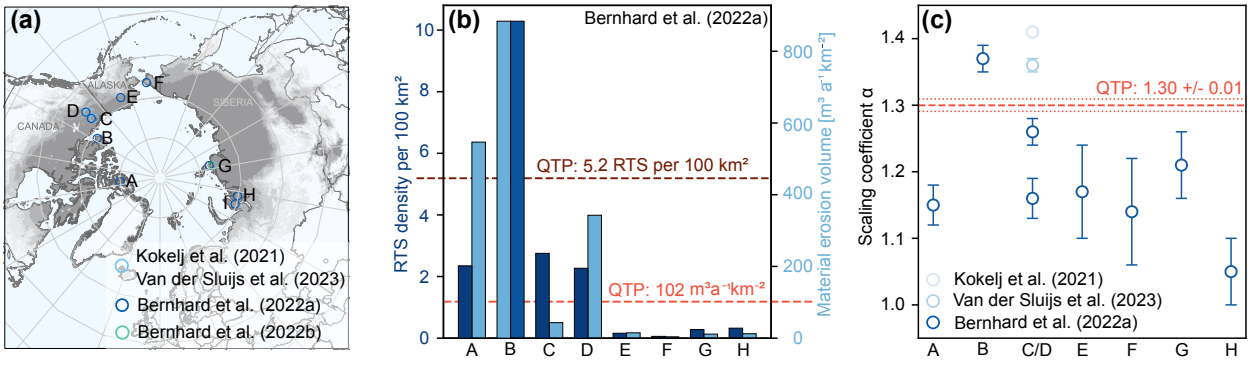

Figure 6. Comparison between RTS in QTP and in Arctic permafrost regions with respect to RTS material erosion and SOC mobilisation. **(a)** Map of Arctic sites investigated by previous studies: Kokelj et al. (2021) and Van Der Sluijs et al. (2023) estimated erosion volume and area-volume scaling for RTS landforms based on high-resolution airborne DEMs in northwestern Canada. Bernhard et al. (2022a) studied RTS area-volume relations based on TanDEM-X DEMs at eight sites in Canada, Alaska and Siberia between 2010 and 2016. Bernhard et al. (2022b) investigated the effects of a summer heatwave on RTS-induced SOC mobilisation in Siberia. **(b)** RTS activity in the QTP is comparable to Arctic sites (Bernhard et al., 2022a): RTS density and erosion volume are consistently higher than the Siberian sites and in the range of the North American thermokarst hotspots. **(c)** Area-volume scaling coefficients α for QTP and Arctic sites: QTP's α-value of 1.30 falls within the range of the investigated Arctic RTS, yet, is closest to the area-volume relation of Banks Island (B) and Peel Plateau (D) in Canada that are both dominated by hillslope RTS compared to many lakeshore RTS in the Siberian sites (F - H).

Allometric scaling has recently been applied to thaw-driven mass wasting to improve understanding of the volumetric enlargement characteristics of RTS and their potential drivers. Kokelj et al. (2021) and Van Der Sluijs et al. (2023) calculated the material erosion volume based on the difference between a high-resolution DEM capturing the disturbed state (T2) and a simulated "pre-disturbance" DEM that represents the terrain before a RTS landform developed (T1) through masking and re-interpolation of the T2 high-resolution DEM. Based on the fitting of a Ordinary Least Square model, the studies estimated α-values of 1.41 (n_{RTS} = 71) for active RTS and 1.36 $\pm$ 0.01 (n_{RTS} = 1,522) for all RTS (including inactive and old landforms) in the Northwestern Territories, Canada (C and D), respectively (Fig. 6 c). The RTS in the investigated sites, Peel Plateau (D) and Tuktoyaktuk Coastlands (c), have significantly different morphologies and mass wasting characteristics (Fig. 6 b). However, the two studies have fitted only one model for all RTS in both sites, while Bernhard et al. (2022a) calculated the power law scaling separately with α = 1.26 $\pm$ 0.02 for Peel Plateau (n_{RTS} = 438) and α = 1.16 $\pm$ 0.03 for the Tuktoyaktuk Coastlands (n_{RTS} = 212). That study, similar to our method, calculates the change in the volume of material erosion between two DEMs from time T1 and T2 and the ablation area visible in the elevation change maps. Except for Banks Island (B, α = 1.37 $\pm$ 0.01, n_{RTS} = 679), Bernhard et al. (2022a) found scaling coefficients below $\alpha < 1.3$ for all other Arctic sites. The power scaling relationship between area and volume for RTS in the QTP (α = 1.30$\pm$ 0.01, n_{RTS} = 3,043) is relatively high compared to

https://doi.org/10.5194/egusphere-2025-2187
Preprint. Discussion started: 17 June 2025

most of the Arctic sites (Fig. 6 c). Xia et al. (2024) found that more than half of the RTS initiated in 2016 (Fig. S2), the first year of the study period, while Luo et al. (2022) found that $>$ 80 % of the investigated RTS in central QTP formed in 2010 and 2016 during extremely warm summers. This would indicate that our scaling results are based on planimetric areas and volumes representing the full RTS landform and its lifecycle similar to the methodology used by Kokelj et al. (2021) and Van Der Sluijs et al. (2023). Since we compute the scaling relation in a log-scale, the computation is very sensitive to only slight differences in the scaling coefficient. A difference of 0.1 in α leads to a factor two increase in the volume estimation (Van Der Sluijs et al., 2023). The areas affected by RTS in this study are generally smaller than in the Arctic (Liu et al., 2024), and have shallowed depth, whereby the resolution of the DEM produced might not correctly capture the area and volume change for these small areas skewing the scaling models. In temperate landslides, it is known that scaling relationships change depending on the average depth of the landslide population (Chen et al., 2019). Furthermore, the mentioned permafrost thaw studies used DEM data from different study periods, a smaller number of samples, and even different methodologies to compute RTS erosion volumes. Area-volume scaling also depends on how the actively eroding RTS scar zone is delineated. While there are commonly accepted definitions of RTS geomorphology (CPA et al., 2024; Harris, 1988), different data sources show different aspects of RTS activity, and even experts working on similar data can differ strongly in their delineations based on their own ontological understandings of what constitute RTS and their past project goals and procedures (Nesterova et al., 2024; Nitze et al., 2024b; Maier et al., 2025).

Therefore, we should only see these results and comparisons as another indicator that RTS development in the QTP is on a level similar to the known hotspots in the Arctic permafrost region. More research is needed, especially on the subregional and local scale, to validate our scaling coefficients with the RTS material erosion data from QTP. When comparing material erosion and area-volume scaling within the QTP subregions, we see almost as strong differences as between the QTP and the Arctic (Fig. 4 a). As Xia et al. (2024) found the highest numbers of RTS clustered in the central QTP, this region also dominates the volume of material erosion. However, the western and northeastern regions have substantially higher α coefficients, indicating larger headwalls and concavity depth per unit area growth. Terrain slope increases towards the west and northeast at RTS locations (Xia et al., 2024), potentially favouring the development of relatively larger and deeper RTS. However, the driving factors underlying the observed differences between the QTP and the Arctic are likely multifaceted, including variations in RTS longevity and lifecycle stage, ground ice content, vegetation and soil properties, or proximity to water bodies. Detailed investigations into these factors remain the subject of prospective research. Our novel dataset offers a critical resource for future investigations into the mechanisms driving RTS mass wasting on the QTP. Our results are consistent with previous observations showing a marked increase in RTS activity across the QTP, particularly over the past decade (Xia et al., 2024, 2022; Luo et al., 2022), but the sizes are generally smaller and the headwall retreat rates are lower than those found in other Arctic regions (Yi et al., 2025; Luo et al., 2022; Lewkowicz and Way, 2019; Runge et al., 2022; Nesterova et al., 2024; Huang et al., 2021). The magnitude of newly formed RTS during the last decade potentially offsets the relatively low concavity depths, so that the total mass-wasting activity and material erosion volume during the last decade show a magnitude comparable to the thermokarst landscapes in the high Arctic.

https://doi.org/10.5194/egusphere-2025-2187
Preprint. Discussion started: 17 June 2025

4.2 Magnitude of SOC mobilisation and effects on the regional carbon budget of QTP

To place our research in context, we compare our estimates of SOC mobilisation with some regional-scale studies on the Taymyr Peninsula in the Siberian Arctic (Bernhard et al., 2022b) and on the Yukon coast in North America (Ramage et al., 2018). Ramage et al. (2018) investigated SOC mobilisation from 49 coastal RTS between 1972 and 2011 from a high-resolution airborne LiDAR DEM and the reconstruction of a pre-disturbance surface (Ramage et al., 2018) while Bernhard et al. (2022b), similar to this study, processed multi-temporal stacks of TanDEM-X-derived DEMs for the time periods 2010 - 2016 (n_{RTS} = 76) and 2017 - 2020 (n_{RTS} = 1404) to investigate the impact of a summer heat wave on hillslope RTS (Table 1).

Table 1. Comparison of QTP estimates on annual SOC mobilisation rates with similar remote sensing studies: Bernhard et al. (2022b) found a strong increase in RTS initiations (17-fold) and SOC mobilisation (28-fold) due to a summer heatwave in 2020 on the Taymyr peninsula in Siberia (Fig. 6 a, location G) between 2011 and 2020. Ramage et al. (2018) investigated the impact on SOC mobilisation from RTS to ocean export in parts of the Yukon coast in the Canadian Arctic between 1972 and 2011.

	Study region	Study period	n_{RTS}	Study area [km^2]	δV [m^3 a^{-1} RTS^{-1}]	SOC mob. density [kg C a^{-1} km^{-2}]	SOC mob. rate [kg C a^{-1} RTS^{-1}]	Contribution of 0 - 1 m depth
Bernhard et al. 2022b	Taymyr, Siberia	2010 - 2016	76	27000	2.3×10^3	450	14.0×10^4	70 %
		2017 - 2020	1404		5.3×10^3	12650	23.4×10^4	75 %
Ramage et al. 2018	Yukon Coast, Canada	1972 - 2011	49	190	0.6×10^3	3741	0.5×10^4	49 %
Our study	QTP	2011 - 2020	3544	68200	1.9×10^3	518	1.1×10^4	75 %

The material erosion volume and SOC mobilisation induced by RTS activity in the QTP show magnitudes relatively similar to the mass wasting of RTS in the Siberian Arctic before the summer when the extreme heat wave occurred. The heat wave triggered a surge in RTS activity with an increase in new initiations (17 times), in the average volume change rate (2.3 times), and in SOC mobilisation (28 times) and resulted in quantities much higher than those observed in the QTP. Comparison with the results of Ramage et al. (2018) is more difficult due to different DEM differencing methods, time frames, SOC stocks, and the definition of the study site. Although the average material erosion rate and the SOC mobilisation rate per RTS is lower than in the QTP, the SOC fluxes normalised by the study area are 7 $\times$ higher for the Yukon coast. However, this can probably be explained by the substantially smaller size of the study area where the authors only accounted for small coastal strips excluding the hinterlands while our study and Bernhard et al. (2022b) focus on broader inland regions. Another substantial difference is the contribution of the uppermost soil layer (0 - 1 m) to the SOC mobilisation. In both QTP and the Taymyr Peninsula, approximately three quarters of the estimated mobilisation of SOC comes from the uppermost metre of soil. On the Yukon coast, approximately half of the mobilised SOC can be accounted for in the upper layer. Possibly, deeper RTS form in the landscape settings of the Canadian Arctic, where RTS activity is tightly interconnected with coastal erosion processes, ground ice distributions, and overall landscape configuration. Furthermore, studies have used different types of data for SOC stocks that likely have a strong influence on the RTS-induced SOC mobilisation estimates.

https://doi.org/10.5194/egusphere-2025-2187
Preprint. Discussion started: 17 June 2025

To our knowledge, no study has quantified the mobilisation of SOC for RTS in QTP. Jiao et al. (2022) investigated one large RTS in the Beiluhe River Basin between 2021 and 2022 and found 1.9 $\mathrm{m\,a^{-1}}$ vertical deformation at the headwall and a total volume change of 1412 $\mathrm{m^3\,a^{-1}}$. The active layer at the RTS location was 1.95 m with a ground ice layer between 2.2 and 3.5 m depth and an ice content of 68 to 88 % at depths of 2.2 to 4 m obtained at a borehole near the RTS. Compared to our results in the central QTP (Fig. 4, Table S1), the investigated RTS has a typical headwall height and material erosion volume ($\overline{\delta h}$ = 1.45 m, δh_{max} = 2.35 m, $\overline{\delta V}$ = 1,971 $\mathrm{m^3\,a^{-1}}$). The measured GI content near the RTS is substantially higher than the average GI content we used in our estimations ($\overline{\mathrm{GI}}$ = 32.4 %). Zou et al. (2024) estimated a ground ice reserve of 3330 $\mathrm{km^3}$ between 2 and 10 m depth peaking in west-central QTP. The GI content is strongly related to the landscape's geomorphology and 85 % is found on gentle shaded slopes at elevations between 4400 and 5100 m (Fan et al., 2023) typical for central subregions and most RTS locations (Fig. S2 b - d). However, some studies also found GI content higher than 80 % in northeast QTP (Wang et al., 2018; Fan et al., 2023) and a mean GI content of $\sim$ 16 % in the Beiluhe River Basin (Lin et al., 2020). RTS only form in locations where massive ground ice is present in depths that can be exposed by, for example, active layer detachments (Nesterova et al., 2024). We might underestimate local ground ice conditions, as we base our calculations on a dataset with a spatial resolution (of 1 $\mathrm{km^2}$) too coarse to capture the heterogeneities present in local ground ice conditions and microtopography (Yi et al., 2025), which in turn could lead to an overestimation of SOC mobilisation.

Parts of the mobilised SOC become available for microbial decomposition and are released as carbon dioxide or methane into the atmosphere (Bröder et al., 2021; Vonk et al., 2013), while a considerable proportion may remain stabilised by mineral interaction and is further sequestered within the redistributing and accumulating sediments, for example, debris tongues (Thomas et al., 2023). Although earth system models do not account for the potential carbon feedbacks from permafrost thaw today, the increasing intensity of Arctic RTS mass wasting is projected to have considerable potential for large contributions to permafrost carbon feedback by the end of the century (Turetsky et al., 2020). However, these projections are highly uncertain, as more recent investigations of large RTS across the pan-Arctic show that the proportion of carbon released by RTS over the last decade is considerably lower than the initial model estimates (Dai et al., in review). From 1961 to 2010, the alpine grasslands in the QTP acted as a carbon sink with a mean annual budget of 101 to 118 $\times\ 10^8\,\mathrm{kg\,C\,a^{-1}}$ (or 10.1 to 11.8 $\mathrm{Tg\,C\,a^{-1}}$) (Piao et al., 2012; Yan et al., 2015). Due to the increase in greening and wetting of the QTP, recent studies even estimate that the QTP region is a carbon sink of 344 $\times\ 10^8\,\mathrm{kg\,C\,a^{-1}}$ (or 34.4 $\mathrm{Tg\,C\,a^{-1}}$) (Chen et al., 2024a; Wang et al., 2023). Our results indicate that RTS-induced SOC mobilisation only accounted for under 1 % of the total carbon budget in the QTP. Although most RTS in the QTP are relatively small and shallow compared to their Arctic counterparts, their rapidly increasing number could become a significant factor in the thawing of previously frozen SOC stocks, especially from the thick carbon-rich active layer, resulting in substantial regional carbon losses. In situ observations from northeast QTP showed a 23 to 37 % loss in surface ($>$ 20 cm) (Mu et al., 2017, 2020; Liu et al., 2018) and slightly less ($\sim$ 20 - 28 %) for SOC stocks in deeper soils (Wu et al., 2018; Yi et al., 2025). Furthermore, vegetation restoration appears to be slower in the QTP than in the Arctic, and exposed areas disturbed by thermokarst can remain bare for decades (Liu et al., 2018; Mu et al., 2017; Li et al., 2025). Wang et al. (2020) estimated for QTP 0.19 to 0.38 $\times\ 10^13\,\mathrm{kg\,C}$ (or 1.9 - 3.8 $\mathrm{Pg\,C}$) from formerly frozen SOC will be subject to decomposition upon permafrost thaw until 2100 under moderate and high-emission climate scenarios that could switch QTP

https://doi.org/10.5194/egusphere-2025-2187
Preprint. Discussion started: 17 June 2025

from a carbon sink to a source. However, these model-based estimations come with large uncertainties, as do our SOC mobilisation estimates for the QTP. Large-scale datasets that estimate SOC stocks and ground ice content in permafrost regions are based on limited observations and also have coarse spatial resolutions that typically do not represent fine-scale soil conditions well (Hugelius et al., 2014; Mishra et al., 2021; Wang et al., 2021; Zou et al., 2024). With increased soil depth, estimates of soil properties become even more scarce (Chen et al., 2024b; Ding et al., 2019). Since we observed negative elevation changes of more than 3 m in RTS in QTP, we used a simple exponential model to extrapolate SOC stocks to deeper soil layers. Probably, this model is too simple and does not capture the spatial variability of soil conditions in the complex permafrost landscape (Bernhard et al., 2022b). However, we found that only 2 % of SOC mobilised by RTS activity contributed to the total loss of SOC stocks at soil depths below 3 m.

Furthermore, the processes and fate of the unfrozen mobilised SOC remain highly uncertain as multiple complex ecosystem interactions and hydrothermal processes are involved (Yi et al., 2025). Parts of mobilised SOC remain on the slump floor and are available for microbial decomposition and release as greenhouse gases (Wang et al., 2024) or deposited and even stabilised (Thomas et al., 2023; Liu et al., 2021, 2018; Mu et al., 2017), while other parts, together with thawed material, are laterally transported downslope into adjacent river and lake systems and SOC can undergo complex water chemistry processes such as dissolution or sedimentation (Lewkowicz and Way, 2019). We only quantified the magnitude of SOC mobilised by RTS activity in QTP over the last decade, and exploring the complex pathways of mobilised SOC is beyond the scope of this study. However, based on the results of our study, we recommend further research into the fate of the mobilised SOC. Figure 5 b clearly shows areas of material ablation, but also regions of material deposition on the slump floor are visible. In future investigations, insights could potentially be generated into how much relocated material and SOC are deposited within an RTS and how much is transported laterally into hydrological networks. In addition, the balance between areas of negative and positive elevation change might be another avenue to improve spatially explicit GI information for the QTP.

4.3 Limitations and Potential of a Multimodal Data Approach for RTS Mass Wasting Monitoring

Compared to the Arctic where the ArcticDEM strip data (Porter et al., 2018) offers an open source and high-resolution multi-temporal DEM source based on stereo-optical satellite images ($\sim$ 3 m) that is suitable for RTS monitoring (Dai et al., 2024; Nitze et al., 2021; Yang et al., 2023), on the QTP no similar high-resolution temporally resolved DEM exists - except for the data from the TanDEM-X mission. Bistatic TanDEM-X observations uniquely enable DEM generation on a global scale. Even in regions with adverse geographic or climatic conditions for satellite remote sensing, e.g., a high percentage of cloud cover or long periods of snow cover, bistatic radar observations can be used to produce high-quality DEMs with acceptable spatial resolution for RTS monitoring (Krieger et al., 2007; Bojarski et al., 2021; Bernhard et al., 2022a; Maier et al., 2025). However, the temporal resolution of TanDEM-X observations is not equal for all regions of the world. Some permafrost regions in the Arctic have been focus areas and DEMs of two to three time steps in the last decade exist. In the QTP, data availability was limited and we had to aggregate observations from several years and seasons to ensure sufficient coverage. For T1, we used observations between mid-winter 2011 and end of winter 2012, while for T2 we had to accept an even larger time span (end of summer 2017 to mid-winter 2020). We can assume that RTS activity only occurs in the warm summer months and a phase

https://doi.org/10.5194/egusphere-2025-2187
Preprint. Discussion started: 17 June 2025

of stability occurs between October and April due to low temperatures (Chen et al., 2015; Che et al., 2008; Ma et al., 2023) so for T2 we have two combined summers (2018 and 2019). However, Xia et al. (2024) found that the highest activity occurred before 2020; afterward, only 59 new RTS were detected on the PlanetScope images. This could indicate that we captured most of the RTS activity that has occurred on the QTP during the last decade. However, to monitor the dynamic lifecycles of these complex thermokarst features and understand their drivers and future development, yearly records of RTS-induced material erosion volumes are highly desirable (Nesterova et al., 2024; Kokelj et al., 2021). The general scarcity of suitable DEM, as well as the temporal limitations, makes monitoring of RTS material erosion and impact on carbon cycles solely based on DEM data challenging. Allometric or area-volume scaling relations, as presented and discussed in this study, are typically used to investigate landscape evolution or RTS activity change over time, but can also be used to enable the investigation of not only planimetric area expansion from optical RTS inventories but also transform the area change into volume change of eroded material and expand the analysis to yearly or even seasonal temporal scales. Our study could for the first time derive a statistically robust scaling relation for the QTP region, similar to regions elsewhere (Bernhard et al., 2022a; Van Der Sluijs et al., 2023; Dai et al., in review). However, a small difference in the scaling coefficient α has a large impact on the resulting volume change δV. We see substantial differences in the scaling relations between the different QTP subregions (Fig. S1 and S3 b - f). When comparing our scaling results with the small number of existing studies on allometric scaling of RTS in the Arctic, we could also see distinct differences between our results and studies investigating similar regions in the Arctic (Bernhard et al., 2022a; Van Der Sluijs et al., 2023; Kokelj et al., 2021). On the QTP, no study, to our best knowledge, has attempted a similar approach due to the lack of high-resolution and multi-temporal DEM data. These limitations highlight that applying such a scaling law to optical RTS inventories should be done carefully and rather to obtain regional estimates on material erosion volume and mass wasting derivatives such as ground ice loss or SOC mobilisation. For subregional scale or even feature level, this approach has its clear limitations due to the heterogeneity of RTS across large but even local scales. However, large-scale and even pan-Arctic RTS inventories based on optical satellite images become more available and may allow for a similar approach of finding scaling relations for Arctic thermokarst regions if delineations coincide well ontologically, spatially and temporally with measured elevation change (Yang et al., 2025b; Nitze et al., 2024a). We could show that remote sensing data with a spatial resolution of $\sim 10\,\mathrm{m}$ misses $\sim 35\,\%$ of RTS features that could be found in higher resolution PlanetScope images which, however, only accounted for a difference of $< 1\,\%$ of the eroded material volume (Fig. 5 c). Open-source and multi-temporal images, such as from ESA's Sentinel-2 satellites, with a similar spatial resolution as TanDEM-X DEMs could have a great potential to continuously monitor RTS activity from the mid of the last decade to answer questions about volumetrics and permafrost thaw impacts on hydrological systems and carbon cycles based on reliable area-volume scaling laws.

5 Conclusions

RTS landforms are typically complex and highly dynamic, often remaining active for several years before stabilising and, in some cases, reinitiating. To adequately capture their temporal evolution and interactions with changing climate, high-temporal-resolution remote sensing data are essential. By combining modelled soil property datasets with multimodal remote sensing

https://doi.org/10.5194/egusphere-2025-2187
Preprint. Discussion started: 17 June 2025

data, we estimated that RTS activity in the QTP between 2011 and 2020 relocated $5.02^{25.35}_{0.75} \times 10^7\,\mathrm{m}^3$ formerly frozen material, contributed to a loss of $3.58^{28.20}_{0.28} \times 10^6\,\mathrm{m}^3$ ground ice and mobilised $2.78^{7.98}_{0.11} \times 10^8\,\mathrm{kg\,C}$ SOC. Interregional comparisons of RTS dynamics are challenging due to varying spatial, temporal, and methodological factors. However, RTS in the QTP exhibit mass-wasting activity comparable to Arctic regions of high RTS activity. Despite their comparably recent initiation and smaller size, QTP erosion and SOC mobilisation in the past decade surpassed some regions in the Siberian Arctic, but remained up to 10 times lower than Canadian high-Arctic hotspots. Although RTS-induced carbon mobilisation represents less than 1 % of QTP's carbon budget, the acceleration of RTS activity since the last decade could contribute to the anticipated shift of the region from a carbon sink to a source. By integrating remote sensing data with varying spatial and temporal resolutions and different information layers, we demonstrated that erosion volumes can be accurately estimated, even when the delineations of the RTS erosion-affected area vary. We found a reliable power law scaling between the area in the optical RTS inventory and the computed material erosion volume change of α = 1.30 $\pm$ 0.01 (R^2 = 0.87 for δA and R^2 = 0.75 for A_{Xia}, p<0.001) that potentially allows future research to transform the planimetric area of RTS delineations into regional estimates of erosion volume and constrain RTS-induced SOC mobilisation on the QTP. Improved estimates and allometric relationships will help close the knowledge gap in understanding the impact of permafrost thaw on the permafrost carbon cycle for the QTP and globally.

Code and data availability. The dataset containing all RTS boundaries of Xia et al. (2024) including the computed active erosion areas, material erosion volumes, ground ice loss, and SOC mobilisation can be found under (https://doi.org/10.3929/ethz-b-000735734. The code and example data for the RTS mass-wasting calculations based on the optical RTS inventory, the validation, and plotting can be found at https://github.com/kathrinmaier/qtp-rts-mass-wasting. TanDEM-X CoSSC data can be requested from the German Aerospace Centre (DLR).

Author contributions. KM, LL, and ZX designed the study. ZX provided the optical RTS labels and produced the photogrammetric validation DEM. KM, PB, and IH developed the methodology. KM prepared the datasets and performed the analysis. IH secured the funding for the study. All co-authors contributed with their specific expertise to data interpretation as well as manuscript writing.

Competing interests. The authors declare that they have no conflict of interest.

Acknowledgements. The authors thank Thomas Busche, Markus Bachmann, and the Order Desk Team at the German Aerospace Centre (DLR) for their help in downloading the large number of TanDEM-X observations in an efficient and timely manner, Dr. Xiaofan Zhu for reviewing an early version of this work, and Chengyan Fan (Lanzhou University) for his support in collecting the VHR drone imagery. Zhuoxuan Xia and Lin Liu were supported by the Hong Kong Research Grants Council (N_CUHK434/21 and CUHK14303119), CUHK

https://doi.org/10.5194/egusphere-2025-2187
Preprint. Discussion started: 17 June 2025

Direct Grant for Research (4053644 and 4053707). Mark Lara was supported by NASA-ABoVE (80NSSC22K1254). Geospatial support for this work was provided by the Polar Geospatial Center under NSF-OPP awards 1043681, 1559691, and 2129685.

https://doi.org/10.5194/egusphere-2025-2187
Preprint. Discussion started: 17 June 2025

References

Bernhard, P., Zwieback, S., Leinss, S., and Hajnsek, I.: Mapping Retrogressive Thaw Slumps Using Single-Pass TanDEM-X Observations, IEEE J. Sel. Top. Appl. Earth Observations Remote Sensing, 13, 3263–3280, https://doi.org/10.1109/JSTARS.2020.3000648, 2020.

Bernhard, P., Zwieback, S., Bergner, N., and Hajnsek, I.: Assessing volumetric change distributions and scaling relations of retrogressive thaw slumps across the Arctic, Cryosphere, 16, 1–15, https://doi.org/10.5194/tc-16-1-2022, 2022a.

Bernhard, P., Zwieback, S., and Hajnsek, I.: Accelerated Mobilization of Organic Carbon from Retrogressive Thaw Slumps on the Northern Taymyr Peninsula, Cryosphere, 16, 2819–2835, https://doi.org/10.5194/tc-2022-36, 2022b.

Biskaborn, B. K., Smith, S. L., Noetzli, J., Matthes, H., Vieira, G., Streletskiy, D. A., Schoeneich, P., Romanovsky, V. E., Lewkowicz, A. G., Abramov, A., Allard, M., Boike, J., Cable, W. L., Christiansen, H. H., Delaloye, R., Diekmann, B., Drozdov, D., Etzelmüller, B., Grosse, G., Guglielmin, M., Ingeman-Nielsen, T., Isaksen, K., Ishikawa, M., Johansson, M., Johannsson, H., Joo, A., Kaverin, D., Kholodov, A., Konstantinov, P., Kröger, T., Lambiel, C., Lanckman, J.-P., Luo, D., Malkova, G., Meiklejohn, I., Moskalenko, N., Oliva, M., Phillips, M., Ramos, M., Sannel, A. B. K., Sergeev, D., Seybold, C., Skryabin, P., Vasiliev, A., Wu, Q., Yoshikawa, K., Zheleznyak, M., and Lantuit, H.: Permafrost is warming at a global scale, Nat. Commun., 10, 264, https://doi.org/10.1038/s41467-018-08240-4, 2019.

Boggs, P. T. and Rogers, J. E.: Orthogonal Distance Regression, Applied and Computational Mathematics Division. U.S. Department of Commerce. National Institute of Standards and Technology, pp. NISTIR 89–4197, 1989.

Bojarski, A., Bachmann, M., Boer, J., Kraus, T., Wecklich, C., Steinbrecher, U., Tous-Ramon, N., Schmidt, K., Klenk, P., Grigorov, C., Schwerdt, M., and Zink, M.: TanDEM-X Long-Term System Performance After 10 Years of Operation, IEEE J. Sel. Top. Appl. Earth Observations Remote Sensing, 14, 2522–2534, https://doi.org/10.1109/JSTARS.2021.3055546, 2021.

Bröder, L., Keskitalo, K., Zolkos, S., Shakil, S., Tank, S. E., Kokelj, S. V., Tesi, T., Van Dongen, B. E., Haghipour, N., Eglinton, T. I., and Vonk, J. E.: Preferential export of permafrost-derived organic matter as retrogressive thaw slumping intensifies, Environmental Research Letters, 16, 054 059, https://doi.org/10.1088/1748-9326/abee4b, 2021.

Burn, C. and Lewkowicz, A.: CANADIAN LANDFORM EXAMPLES - 17 RETROGRESSIVE THAW SLUMPS, Canadian Geographer, 34, 273–276, https://doi.org/10.1111/j.1541-0064.1990.tb01092.x, 1990.

Che, T., Li, X., Jin, R., Armstrong, R., and Zhang, T.: Snow depth derived from passive microwave remote-sensing data in China, Annals of Glaciology, 49, 145–154, https://doi.org/10.3189/172756408787814690, 2008.

Chen, L., Yang, G., Bai, Y., Chang, J., Qin, S., Liu, F., He, M., Song, Y., Zhang, F., Peñuelas, J., Zhu, B., Zhou, G., and Yang, Y.: Permafrost carbon cycle and its dynamics on the Tibetan Plateau, Science China Life Sciences, 67, 1833–1848, https://doi.org/10.1007/s11427-023-2601-1, 2024a.

Chen, S.-c., Chen, C.-y., and Huang, W.-y.: Exploring landslide erosion volume–area scaling relationships by slip depth using changes in DTMs for basin sediment volume estimation, Journal of Mountain Science, 16, 581–594, https://doi.org/10.1007/s11629-018-4888-3, 2019.

Chen, T., Wang, J., Che, T., Hao, X., and Li, H.: High spatial resolution elevation change dataset derived from ICESat-2 crossover points on the Tibetan Plateau, Scientific Data, 11, 394, https://doi.org/10.1038/s41597-024-03214-2, 2024b.

Chen, X., An, S., Inouye, D. W., and Schwartz, M. D.: Temperature and snowfall trigger alpine vegetation green-up on the world's roof, Global Change Biology, 21, 3635–3646, https://doi.org/10.1111/gcb.12954, 2015.

Cheng, G. and Wu, T.: Responses of permafrost to climate change and their environmental significance, Qinghai-Tibet Plateau, Journal of Geophysical Research: Earth Surface, 112, 2006JF000 631, https://doi.org/10.1029/2006JF000631, 2007.

https://doi.org/10.5194/egusphere-2025-2187
Preprint. Discussion started: 17 June 2025

CPA, Lewkowicz, A., Wolfe, S., Geological Survey of Canada, Roujanski, V., Tetra Tech Canada, Hoeve, E., HoeveEng Consulting Ltd, O'Neill, B., Geological Survey of Canada, Gruber, S., Carleton University, Roy-Léveillée, P., Université Laval, Brown, N., Carleton University, Koenig, C., BGC Engineering, Brooks, H., BGC Engineering, Rudy, A., Northwest Territories Geological Survey, Bonnaventure, P., University of Lethbridge, Paquette, M., and Stantec: An Illustrated Permafrost Dictionary, Tech. rep., https://doi.org/10.52381/CPA.permafrostdictionary.1, 2024.

Dai, C., Howat, I. M., Van Der Sluijs, J., Liljedahl, A. K., Higman, B., Freymueller, J. T., Ward Jones, M. K., Kokelj, S. V., Boike, J., Walker, B., and Marsh, P.: Applications of ArcticDEM for measuring volcanic dynamics, landslides, retrogressive thaw slumps, snowdrifts, and vegetation heights, Science of Remote Sensing, 9, 100 130, https://doi.org/10.1016/j.srs.2024.100130, 2024.

Dai, C., Ward Jones, M., Van Der Sluijs, J., Nesterova, N., Howat, I. M., Liljedahl, A., Higman, B., Freymueller, J., Kokelj, S. V., and Sriram, S.: Volumetric Quantifications and Dynamics of Areas Undergoing Retrogressive Thaw Slumping in the Northern Hemisphere Between 2012 and 2022, in review.

Ding, J., Wang, T., Piao, S., Smith, P., Zhang, G., Yan, Z., Ren, S., Liu, D., Wang, S., Chen, S., Dai, F., He, J., Li, Y., Liu, Y., Mao, J., Arain, A., Tian, H., Shi, X., Yang, Y., Zeng, N., and Zhao, L.: The paleoclimatic footprint in the soil carbon stock of the Tibetan permafrost region, Nature Communications, 10, 4195, https://doi.org/10.1038/s41467-019-12214-5, 2019.

Fan, X., Wang, Y., Niu, F., Li, W., Wu, X., Ding, Z., Pang, W., and Lin, Z.: Environmental Characteristics of High Ice-Content Permafrost on the Qinghai–Tibetan Plateau, Remote Sensing, 15, 4496, https://doi.org/10.3390/rs15184496, 2023.

Farquharson, L. M., Romanovsky, V. E., Cable, W. L., Walker, D. A., Kokelj, S. V., and Nicolsky, D.: Climate Change Drives Widespread and Rapid Thermokarst Development in Very Cold Permafrost in the Canadian High Arctic, Geophysical Research Letters, 46, 6681–6689, https://doi.org/10.1029/2019GL082187, 2019.

Grosse, G., Harden, J., Turetsky, M., McGuire, A. D., Camill, P., Tarnocai, C., Frolking, S., Schuur, E. A. G., Jorgenson, T., Marchenko, S., Romanovsky, V., Wickland, K. P., French, N., Waldrop, M., Bourgeau-Chavez, L., and Striegl, R. G.: Vulnerability of high-latitude soil organic carbon in North America to disturbance, J. Geophys. Res., 116, https://doi.org/10.1029/2010JG001507, 2011.

Günther, F., Overduin, P. P., Yakshina, I. A., Opel, T., Baranskaya, A. V., and Grigoriev, M. N.: Observing Muostakh disappear: permafrost thaw subsidence and erosion of a ground-ice-rich island in response to arctic summer warming and sea ice reduction, The Cryosphere, 9, 151–178, https://doi.org/10.5194/tc-9-151-2015, 2015.

Hall, E., Chipman, M., and Lara, M.: Predicting Retrogressive Thaw Slump expansion across northern Alaska, in review.

Harris, S. A., ed.: Glossary of permafrost and related ground-ice terms, no. 142 in Technical Memorandum / National Research Council, Canada, Ottawa, Ontario, Canada, ISBN 978-0-660-12540-4, 1988.

Hjort, J., Streletskiy, D., Doré, G., Wu, Q., Bjella, K., and Luoto, M.: Impacts of permafrost degradation on infrastructure, Nature Reviews Earth & Environment, 3, 24–38, https://doi.org/10.1038/s43017-021-00247-8, 2022.

Holloway, J. E., Lewkowicz, A. G., Douglas, T. A., Li, X., Turetsky, M. R., Baltzer, J. L., and Jin, H.: Impact of wildfire on permafrost landscapes: A review of recent advances and future prospects, Permafrost and Periglacial Processes, 31, 371–382, https://doi.org/10.1002/ppp.2048, 2020.

Huang, L., Luo, J., Lin, Z., Niu, F., and Liu, L.: Using deep learning to map retrogressive thaw slumps in the Beiluhe region (Tibetan Plateau) from CubeSat images, Remote Sensing of Environment, 237, 111 534, https://doi.org/10.1016/j.rse.2019.111534, 2020.

Huang, L., Liu, L., Luo, J., Lin, Z., and Niu, F.: Automatically quantifying evolution of retrogressive thaw slumps in Beiluhe (Tibetan Plateau) from multi-temporal CubeSat images, International Journal of Applied Earth Observation and Geoinformation, 102, 102 399, https://doi.org/10.1016/j.jag.2021.102399, 2021.

https://doi.org/10.5194/egusphere-2025-2187
Preprint. Discussion started: 17 June 2025

Hugelius, G., Strauss, J., Zubrzycki, S., Harden, J. W., Schuur, E. A. G., Ping, C.-L., Schirrmeister, L., Grosse, G., Michaelson, G. J., Koven, C. D., O'Donnell, J. A., Elberling, B., Mishra, U., Camill, P., Yu, Z., Palmtag, J., and Kuhry, P.: Estimated stocks of circumpolar permafrost carbon with quantified uncertainty ranges and identified data gaps, Biogeosciences, 11, 6573–6593, https://doi.org/10.5194/bg-11-6573-2014, 2014.

Hugonnet, R., Mannerfelt, E., Dehecq, A., Knuth, F., and Tedstone, A.: xDEM, https://doi.org/10.5281/ZENODO.4809698, 2021.

Jaboyedoff, M., Carrea, D., Derron, M.-H., Oppikofer, T., Penna, I. M., and Rudaz, B.: A review of methods used to estimate initial landslide failure surface depths and volumes, Engineering Geology, 267, 105 478, https://doi.org/10.1016/j.enggeo.2020.105478, 2020.

Jiao, C., Niu, F., He, P., Ren, L., Luo, J., and Shan, Y.: Deformation and Volumetric Change in a Typical Retrogressive Thaw Slump in Permafrost Regions of the Central Tibetan Plateau, China, Remote Sensing, 14, 5592, https://doi.org/10.3390/rs14215592, 2022.

Kokelj, S., Tunnicliffe, J., Lacelle, D., Lantz, T., Chin, K., and Fraser, R.: Increased precipitation drives mega slump development and destabilization of ice-rich permafrost terrain, northwestern Canada, Global and Planetary Change, 129, 56–68, https://doi.org/10.1016/j.gloplacha.2015.02.008, 2015.

Kokelj, S. V. and Jorgenson, M. T.: Advances in Thermokarst Research, Permafr. Periglac. Process., 24, 108–119, https://doi.org/10.1002/ppp.1779, 2013.

Kokelj, S. V., Kokoszka, J., van der Sluijs, J., Rudy, A. C. A., Tunnicliffe, J., Shakil, S., Tank, S. E., and Zolkos, S.: Thaw-driven mass wasting couples slopes with downstream systems, and effects propagate through Arctic drainage networks, The Cryosphere, 15, 3059–3081, https://doi.org/10.5194/tc-15-3059-2021, 2021.

Krautblatter, M., Angelopoulos, M., Pollard, W. H., Lantuit, H., Lenz, J., Fritz, M., Couture, N., and Eppinger, S.: Life Cycles and Polycyclicity of Mega Retrogressive Thaw Slumps in Arctic Permafrost Revealed by 2D/3D Geophysics and Long-Term Retreat Monitoring, Journal of Geophysical Research: Earth Surface, 129, e2023JF007 556, https://doi.org/10.1029/2023JF007556, 2024.

Krieger, G., Moreira, A., Fiedler, H., Hajnsek, I., Werner, M., Younis, M., and Zink, M.: TanDEM-X: A Satellite Formation for High-Resolution SAR Interferometry, IEEE Trans. Geosci. Remote Sens., 45, 3317–3341, https://doi.org/10.1109/TGRS.2007.900693, 2007.

Lantuit, H. and Pollard, W. H.: Temporal stereophotogrammetric analysis of retrogressive thaw slumps on Herschel Island, Yukon Territory, Natural Hazards and Earth System Sciences, 5, 413–423, https://doi.org/10.5194/nhess-5-413-2005, 2005.

Lantz, T. C. and Kokelj, S. V.: Increasing rates of retrogressive thaw slump activity in the Mackenzie Delta region, N.W.T., Canada, Geophys. Res. Lett., 35, L06 502, https://doi.org/10.1029/2007GL032433, 2008.

Leinss, S. and Bernhard, P.: TanDEM-X: Deriving InSAR Height Changes and Velocity Dynamics of Great Aletsch Glacier, IEEE J. Sel. Top. Appl. Earth Observations Remote Sensing, 14, 4798–4815, https://doi.org/10.1109/JSTARS.2021.3078084, 2021.

Lewkowicz, A. G. and Way, R. G.: Extremes of summer climate trigger thousands of thermokarst landslides in a High Arctic environment, Nat. Commun., 10, 1329, https://doi.org/10.1038/s41467-019-09314-7, 2019.

Li, D., Lu, X., Walling, D. E., Zhang, T., Steiner, J. F., Wasson, R. J., Harrison, S., Nepal, S., Nie, Y., Immerzeel, W. W., Shugar, D. H., Koppes, M., Lane, S., Zeng, Z., Sun, X., Yegorov, A., and Bolch, T.: High Mountain Asia hydropower systems threatened by climate-driven landscape instability, Nature Geoscience, 15, 520–530, https://doi.org/10.1038/s41561-022-00953-y, 2022.

Li, W., Yan, D., Lou, Y., Weng, B., Zhu, L., Lai, Y., and Wang, Y.: Characteristic, relationship and impact of thermokarst lakes and retrogressive thaw slumps over the Qinghai-Tibetan plateau, Geoderma, 457, 117 293, https://doi.org/10.1016/j.geoderma.2025.117293, 2025.

Lin, Z., Gao, Z., Fan, X., Niu, F., Luo, J., Yin, G., and Liu, M.: Factors controlling near surface ground-ice characteristics in a region of warm permafrost, Beiluhe Basin, Qinghai-Tibet Plateau, Geoderma, 376, 114 540, https://doi.org/10.1016/j.geoderma.2020.114540, 2020.

https://doi.org/10.5194/egusphere-2025-2187
Preprint. Discussion started: 17 June 2025

Liu, F., Chen, L., Abbott, B. W., Xu, Y., Yang, G., Kou, D., Qin, S., Strauss, J., Wang, Y., Zhang, B., and Yang, Y.: Reduced quantity and quality of SOM along a thaw sequence on the Tibetan Plateau, Environmental Research Letters, 13, 104 017, https://doi.org/10.1088/1748-9326/aae43b, 2018.

Liu, F., Kou, D., Chen, Y., Xue, K., Ernakovich, J. G., Chen, L., Yang, G., and Yang, Y.: Altered microbial structure and function after thermokarst formation, Global Change Biology, 27, 823–835, https://doi.org/10.1111/gcb.15438, 2021.

Liu, X. and Chen, B.: Climatic warming in the Tibetan Plateau during recent decades, International Journal of Climatology, 20, 1729–1742, https://doi.org/10.1002/1097-0088(20001130)20:14<1729::AID-JOC556>3.0.CO;2-Y, 2000.

Liu, Y., Qiu, H., Kamp, U., Wang, N., Wang, J., Huang, C., and Tang, B.: Higher temperature sensitivity of retrogressive thaw slump activity in the Arctic compared to the Third Pole, Science of The Total Environment, 914, 170 007, https://doi.org/10.1016/j.scitotenv.2024.170007, 2024.

Luo, J., Niu, F., Lin, Z., Liu, M., and Yin, G.: Recent acceleration of thaw slumping in permafrost terrain of Qinghai-Tibet Plateau: An example from the Beiluhe Region, Geomorphology, 341, 79–85, https://doi.org/10.1016/j.geomorph.2019.05.020, 2019.

Luo, J., Niu, F., Lin, Z., Liu, M., Yin, G., and Gao, Z.: Inventory and Frequency of Retrogressive Thaw Slumps in Permafrost Region of the Qinghai–Tibet Plateau, Geophysical Research Letters, 49, https://doi.org/10.1029/2022GL099829, 2022.

Ma, Y., Huang, X.-D., Yang, X.-L., Li, Y.-X., Wang, Y.-L., and Liang, T.-G.: Mapping snow depth distribution from 1980 to 2020 on the tibetan plateau using multi-source remote sensing data and downscaling techniques, ISPRS Journal of Photogrammetry and Remote Sensing, 205, 246–262, https://doi.org/10.1016/j.isprsjprs.2023.10.012, 2023.

Maier, K., Bernhard, P., Ly, S., Volpi, M., Nitze, I., Li, S., and Hajnsek, I.: Detecting mass wasting of Retrogressive Thaw Slumps in spaceborne elevation models using deep learning, International Journal of Applied Earth Observation and Geoinformation, 137, 104 419, https://doi.org/10.1016/j.jag.2025.104419, 2025.

Martone, M., Bräutigam, B., Rizzoli, P., Gonzalez, C., Bachmann, M., and Krieger, G.: Coherence evaluation of TanDEM-X interferometric data, ISPRS J. Photogramm. Remote Sens., 73, 21–29, https://doi.org/10.1016/j.isprsjprs.2012.06.006, 2012.

Millan, R., Dehecq, A., Trouve, E., Gourmelen, N., and Berthier, E.: Elevation changes and X-band ice and snow penetration inferred from TanDEM-X data of the Mont-Blanc area, in: 8th International Workshop on the Analysis of Multitemporal Remote Sensing Images (Multi-Temp), pp. 1–4, https://doi.org/10.1109/Multi-Temp.2015.7245753, 2015.

Mishra, U., Hugelius, G., Shelef, E., Yang, Y., Strauss, J., Lupachev, A., Harden, J. W., Jastrow, J. D., Ping, C.-L., Riley, W. J., Schuur, E. A. G., Matamala, R., Siewert, M., Nave, L. E., Koven, C. D., Fuchs, M., Palmtag, J., Kuhry, P., Treat, C. C., Zubrzycki, S., Hoffman, F. M., Elberling, B., Camill, P., Veremeeva, A., and Orr, A.: Spatial heterogeneity and environmental predictors of permafrost region soil organic carbon stocks, Science Advances, 7, eaaz5236, https://doi.org/10.1126/sciadv.aaz5236, 2021.

Mu, C., Abbott, B. W., Norris, A. J., Mu, M., Fan, C., Chen, X., Jia, L., Yang, R., Zhang, T., Wang, K., Peng, X., Wu, Q., Guggenberger, G., and Wu, X.: The status and stability of permafrost carbon on the Tibetan Plateau, Earth-Science Reviews, 211, 103 433, https://doi.org/10.1016/j.earscirev.2020.103433, 2020.

Mu, C. C., Abbott, B. W., Zhao, Q., Su, H., Wang, S. F., Wu, Q. B., Zhang, T. J., and Wu, X. D.: Permafrost collapse shifts alpine tundra to a carbon source but reduces N_2 O and CH_4 release on the northern Qinghai-Tibetan Plateau, Geophysical Research Letters, 44, 8945–8952, https://doi.org/10.1002/2017GL074338, 2017.

Nesterova, N., Khomutov, A., Kalyukina, A., and Leibman, M.: The specificity of thermal denudation feature distribution on Yamal and Gydan peninsulas, Russia, in: EGU General Assembly 2020, Online, 4–8 May 2020, https://doi.org/10.5194/egusphere-egu2020-746, 2020.

https://doi.org/10.5194/egusphere-2025-2187
Preprint. Discussion started: 17 June 2025

Nesterova, N., Leibman, M., Kizyakov, A., Lantuit, H., Tarasevich, I., Nitze, I., Veremeeva, A., and Grosse, G.: Review article: Retrogressive thaw slump characteristics and terminology, The Cryosphere, 18, 4787–4810, https://doi.org/10.5194/tc-18-4787-2024, 2024.

Nitzbon, J., Westermann, S., Langer, M., Martin, L. C. P., Strauss, J., Laboor, S., and Boike, J.: Fast response of cold ice-rich permafrost in northeast Siberia to a warming climate, Nature Communications, 11, 2201, https://doi.org/10.1038/s41467-020-15725-8, 2020.

Nitze, I., Heidler, K., Barth, S., and Grosse, G.: Developing and Testing a Deep Learning Approach for Mapping Retrogressive Thaw Slumps, Remote Sensing, 13, 4294, https://doi.org/10.3390/rs13214294, 2021.

Nitze, I., Heidler, K., Nesterova, N., Küpper, J., Schütt, E., Hölzer, T., Barth, S., Lara, M., Liljedahl, A., and Grosse, G.: DARTS: Multi-year database of AI-detected retrogressive thaw slumps in the circum-arctic permafrost region, https://doi.org/10.31223/X5740Z, preprint, 2024a.

Nitze, I., Van der Sluijs, J., Barth, S., Bernhard, P., Huang, L., Kizyakov, A., Lara, M., Nesterova, N., Runge, A., Veremeeva, A., Ward Jones, M., Witharana, C., Xia, Z., and Liljedahl, A.: A Labeling Intercomparison of Retrogressive Thaw Slumps by a Diverse Group of Domain Experts, Permafr. Periglac. Process., p. 2249, https://doi.org/10.1002/ppp.2249, 2024b.

O'Neill, H. B., Smith, S. L., Burn, C. R., Duchesne, C., and Zhang, Y.: Widespread Permafrost Degradation and Thaw Subsidence in Northwest Canada, Journal of Geophysical Research: Earth Surface, 128, e2023JF007 262, https://doi.org/10.1029/2023JF007262, 2023.

Piao, S., Tan, K., Nan, H., Ciais, P., Fang, J., Wang, T., Vuichard, N., and Zhu, B.: Impacts of climate and CO2 changes on the vegetation growth and carbon balance of Qinghai–Tibetan grasslands over the past five decades, Global and Planetary Change, 98-99, 73–80, https://doi.org/10.1016/j.gloplacha.2012.08.009, 2012.

Porter, C., Morin, P., Howat, I., Noh, M.-J., Bates, B., Peterman, K., Keesey, S., Schlenk, M., Gardiner, J., Tomko, K., Willis, M., Kelleher, C., Cloutier, M., Husby, E., Foga, S., Nakamura, H., Platson, M., Wethington, M., Williamson, C., Bauer, G., Enos, J., Arnold, G., Kramer, W., Becker, P., Doshi, A., D'Souza, C., Cummens, P., Laurier, F., and Bojesen, M.: ArcticDEM, Version 3, https://doi.org/10.7910/DVN/OHHUKH, 2018.

Ramage, J. L., Irrgang, A. M., Morgenstern, A., and Lantuit, H.: Increasing coastal slump activity impacts the release of sediment and organic carbon into the Arctic Ocean, Biogeosciences, 15, 1483–1495, https://doi.org/10.5194/bg-15-1483-2018, 2018.

Ran, Y., Li, X., Cheng, G., Che, J., Aalto, J., Karjalainen, O., Hjort, J., Luoto, M., Jin, H., Obu, J., Hori, M., Yu, Q., and Chang, X.: New high-resolution estimates of the permafrost thermal state and hydrothermal conditions over the Northern Hemisphere, Earth System Science Data, 14, 865–884, https://doi.org/10.5194/essd-14-865-2022, 2022.

Rodriguez, E. and Martin, J.: Theory and design of interferometric synthetic aperture radars, IEE Proceedings F Radar and Signal Processing, 139, 147, https://doi.org/10.1049/ip-f-2.1992.0018, 1992.

Rosen, P., Hensley, S., Joughin, I., Li, F., Madsen, S., Rodriguez, E., and Goldstein, R.: Synthetic aperture radar interferometry, Proceedings of the IEEE, 88, 333–382, https://doi.org/10.1109/5.838084, 2000.

Runge, A., Nitze, I., and Grosse, G.: Remote sensing annual dynamics of rapid permafrost thaw disturbances with LandTrendr, Remote Sens. Environ., 268, 112 752, https://doi.org/10.1016/j.rse.2021.112752, 2022.

Schuur, E. A., Abbott, B. W., Commane, R., Ernakovich, J., Euskirchen, E., Hugelius, G., Grosse, G., Jones, M., Koven, C., Leshyk, V., Lawrence, D., Loranty, M. M., Mauritz, M., Olefeldt, D., Natali, S., Rodenhizer, H., Salmon, V., Schädel, C., Strauss, J., Treat, C., and Turetsky, M.: Permafrost and Climate Change: Carbon Cycle Feedbacks From the Warming Arctic, Annual Review of Environment and Resources, 47, 343–371, https://doi.org/10.1146/annurev-environ-012220-011847, 2022.

https://doi.org/10.5194/egusphere-2025-2187
Preprint. Discussion started: 17 June 2025

Schuur, E. a. G., McGuire, A. D., Schädel, C., Grosse, G., Harden, J. W., Hayes, D. J., Hugelius, G., Koven, C. D., Kuhry, P., Lawrence, D. M., Natali, S. M., Olefeldt, D., Romanovsky, V. E., Schaefer, K., Turetsky, M. R., Treat, C. C., and Vonk, J. E.: Climate change and the permafrost carbon feedback, Nature, 520, 171–179, https://doi.org/10.1038/nature14338, 2015.

Smith, S. L., O'Neill, H. B., Isaksen, K., Noetzli, J., and Romanovsky, V. E.: The changing thermal state of permafrost, Nature Reviews Earth & Environment, 3, 10–23, https://doi.org/10.1038/s43017-021-00240-1, 2022.

Thomas, M., Monhonval, A., Hirst, C., Bröder, L., Zolkos, S., Vonk, J. E., Tank, S. E., Keskitalo, K. H., Shakil, S., Kokelj, S. V., Van Der Sluijs, J., and Opfergelt, S.: Evidence for preservation of organic carbon interacting with iron in material displaced from retrogressive thaw slumps: Case study in Peel Plateau, western Canadian Arctic, Geoderma, 433, 116 443, https://doi.org/10.1016/j.geoderma.2023.116443, 2023.

Tunnicliffe, J. F., Kokelj, S. V., and Van Der Sluijs, J.: Retrogressive thaw (mega-) slumps within an incised plateau: materials, process, and rates, in preparation.

Turetsky, M. R., Abbott, B. W., Jones, M. C., Anthony, K. W., Olefeldt, D., Schuur, E. A. G., Grosse, G., Kuhry, P., Hugelius, G., Koven, C., Lawrence, D. M., Gibson, C., Sannel, A. B. K., and McGuire, A. D.: Carbon release through abrupt permafrost thaw, Nat. Geosci., 13, 138–143, https://doi.org/10.1038/s41561-019-0526-0, 2020.

Van Der Sluijs, J., Kokelj, S. V., Fraser, R. H., Tunnicliffe, J., and Lacelle, D.: Permafrost Terrain Dynamics and Infrastructure Impacts Revealed by UAV Photogrammetry and Thermal Imaging, Remote Sensing, 10, 1734, https://doi.org/10.3390/rs10111734, 2018.

Van Der Sluijs, J., Kokelj, S. V., and Tunnicliffe, J. F.: Allometric scaling of retrogressive thaw slumps, Cryosphere, 17, 4511–4533, https://doi.org/10.5194/tc-17-4511-2023, 2023.

Virkkala, A., Aalto, J., Rogers, B. M., Tagesson, T., Treat, C. C., Natali, S. M., Watts, J. D., Potter, S., Lehtonen, A., Mauritz, M., Schuur, E. A. G., Kochendorfer, J., Zona, D., Oechel, W., Kobayashi, H., Humphreys, E., Goeckede, M., Iwata, H., Lafleur, P. M., Euskirchen, E. S., Bokhorst, S., Marushchak, M., Martikainen, P. J., Elberling, B., Voigt, C., Biasi, C., Sonnentag, O., Parmentier, F. W., Ueyama, M., Celis, G., St.Louis, V. L., Emmerton, C. A., Peichl, M., Chi, J., Järveoja, J., Nilsson, M. B., Oberbauer, S. F., Torn, M. S., Park, S., Dolman, H., Mammarella, I., Chae, N., Poyatos, R., López-Blanco, E., Christensen, T. R., Kwon, M. J., Sachs, T., Holl, D., and Luoto, M.: Statistical upscaling of ecosystem CO_2 fluxes across the terrestrial tundra and boreal domain: Regional patterns and uncertainties, Global Change Biology, 27, 4040–4059, https://doi.org/10.1111/gcb.15659, 2021.

Vonk, J. E., Mann, P. J., Davydov, S., Davydova, A., Spencer, R. G. M., Schade, J., Sobczak, W. V., Zimov, N., Zimov, S., Bulygina, E., Eglinton, T. I., and Holmes, R. M.: High biolability of ancient permafrost carbon upon thaw, Geophysical Research Letters, 40, 2689–2693, https://doi.org/10.1002/grl.50348, 2013.

Wang, B. and French, H. M.: Climate controls and high-altitude permafrost, qinghai-xizang (tibet) Plateau, China, Permafrost and Periglacial Processes, 5, 87–100, https://doi.org/10.1002/ppp.3430050203, 1994.

Wang, D., Wu, T., Zhao, L., Mu, C., Li, R., Wei, X., Hu, G., Zou, D., Zhu, X., Chen, J., Hao, J., Ni, J., Li, X., Ma, W., Wen, A., Shang, C., La, Y., Ma, X., and Wu, X.: A 1 km resolution soil organic carbon dataset for frozen ground in the Third Pole, Earth System Science Data, 13, 3453–3465, https://doi.org/10.5194/essd-13-3453-2021, 2021.

Wang, G., Peng, Y., Chen, L., Abbott, B. W., Ciais, P., Kang, L., Liu, Y., Li, Q., Peñuelas, J., Qin, S., Smith, P., Song, Y., Strauss, J., Wang, J., Wei, B., Yu, J., Zhang, D., and Yang, Y.: Enhanced response of soil respiration to experimental warming upon thermokarst formation, Nature Geoscience, 17, 532–538, https://doi.org/10.1038/s41561-024-01440-2, 2024.

Wang, S., Sheng, Y., Li, J., Wu, J., Cao, W., and Ma, S.: An Estimation of Ground Ice Volumes in Permafrost Layers in Northeastern Qinghai-Tibet Plateau, China, Chinese Geographical Science, 28, 61–73, https://doi.org/10.1007/s11769-018-0932-z, 2018.

https://doi.org/10.5194/egusphere-2025-2187
Preprint. Discussion started: 17 June 2025

Wang, T., Yang, D., Yang, Y., Piao, S., Li, X., Cheng, G., and Fu, B.: Permafrost thawing puts the frozen carbon at risk over the Tibetan Plateau, Science Advances, 6, eaaz3513, https://doi.org/10.1126/sciadv.aaz3513, 2020.

Wang, X., Ran, Y., Pang, G., Chen, D., Su, B., Chen, R., Li, X., Chen, H. W., Yang, M., Gou, X., Jorgenson, M. T., Aalto, J., Li, R., Peng, X., Wu, T., Clow, G. D., Wan, G., Wu, X., and Luo, D.: Contrasting characteristics, changes, and linkages of permafrost between the Arctic and the Third Pole, Earth-Science Reviews, 230, 104 042, https://doi.org/10.1016/j.earscirev.2022.104042, 2022.

Wang, Y., Xiao, J., Ma, Y., Ding, J., Chen, X., Ding, Z., and Luo, Y.: Persistent and enhanced carbon sequestration capacity of alpine grasslands on Earth's Third Pole, Science Advances, 9, eade6875, https://doi.org/10.1126/sciadv.ade6875, 2023.

Wang, Z.-w., Wang, Q., Zhao, L., Wu, X.-d., Yue, G.-y., Zou, D.-f., Nan, Z.-t., Liu, G.-y., Pang, Q.-q., Fang, H.-b., Wu, T.-h., Shi, J.-z., Jiao, K.-q., Zhao, Y.-h., and Zhang, L.-l.: Mapping the vegetation distribution of the permafrost zone on the Qinghai-Tibet Plateau, Journal of Mountain Science, 13, 1035–1046, https://doi.org/10.1007/s11629-015-3485-y, 2016.

Werner, C., Wegmüller, U., Strozzi, T., and Wiesmann, A.: GAMMA SAR AND INTERFEROMETRIC PROCESSING SOFTWARE, in: European Space Agency (Special Publication) ESA SP, vol. 461, pp. 211–219, 2000.

Wu, Q. and Zhang, T.: Recent permafrost warming on the Qinghai-Tibetan Plateau, Journal of Geophysical Research: Atmospheres, 113, 2007JD009 539, https://doi.org/10.1029/2007JD009539, 2008.

Wu, X., Xu, H., Liu, G., Zhao, L., and Mu, C.: Effects of permafrost collapse on soil bacterial communities in a wet meadow on the northern Qinghai-Tibetan Plateau, BMC Ecology, 18, 27, https://doi.org/10.1186/s12898-018-0183-y, 2018.

Xia, Z., Huang, L., Fan, C., Jia, S., Lin, Z., Liu, L., Luo, J., Niu, F., and Zhang, T.: Retrogressive thaw slumps along the Qinghai–Tibet Engineering Corridor: a comprehensive inventory and their distribution characteristics, Earth Syst. Sci. Data, 14, 3875–3887, https://doi.org/10.5194/essd-14-3875-2022, 2022.

Xia, Z., Liu, L., Mu, C., Peng, X., Zhao, Z., Huang, L., Luo, J., and Fan, C.: Widespread and Rapid Activities of Retrogressive Thaw Slumps on the Qinghai-Tibet Plateau From 2016 to 2022, Geophysical Research Letters, 51, e2024GL109 616, https://doi.org/10.1029/2024GL109616, 2024.

Yan, L., Zhou, G., Wang, Y., Hu, T., and Sui, X.: The spatial and temporal dynamics of carbon budget in the alpine grasslands on the Qinghai-Tibetan Plateau using the Terrestrial Ecosystem Model, Journal of Cleaner Production, 107, 195–201, https://doi.org/10.1016/j.jclepro.2015.04.140, 2015.

Yang, G., Qiu, H., Wang, N., Yang, D., and Liu, Y.: Tracking 35-year dynamics of retrogressive thaw slumps across permafrost regions of the Tibetan Plateau, Remote Sensing of Environment, 325, 114 786, https://doi.org/10.1016/j.rse.2025.114786, 2025a.

Yang, J., Jiang, L., Luojus, K., Pan, J., Lemmetyinen, J., Takala, M., and Wu, S.: Snow depth estimation and historical data reconstruction over China based on a random forest machine learning approach, The Cryosphere, 14, 1763–1778, https://doi.org/10.5194/tc-14-1763-2020, 2020.

Yang, Y., Rogers, B. M., Fiske, G., Watts, J., Potter, S., Windholz, T., Mullen, A., Nitze, I., and Natali, S. M.: Mapping retrogressive thaw slumps using deep neural networks, Remote Sens. Environ., 288, 113 495, https://doi.org/10.1016/j.rse.2023.113495, 2023.

Yang, Y., Rodenhizer, H., Rogers, B. M., Dean, J., Singh, R., Windholz, T., Poston, A., Potter, S., Zolkos, S., Fiske, G., Watts, J., Huang, L., Witharana, C., Nitze, I., Nesterova, N., Barth, S., Grosse, G., Lantz, T., Runge, A., Lombardo, L., Nicu, I. C., Rubensdotter, L., Makopoulou, E., and Natali, S.: A Collaborative and Scalable Geospatial Data Set for Arctic Retrogressive Thaw Slumps with Data Standards, Scientific Data, 12, 18, https://doi.org/10.1038/s41597-025-04372-7, 2025b.

Yao, T., Xue, Y., Chen, D., Chen, F., Thompson, L., Cui, P., Koike, T., Lau, W. K.-M., Lettenmaier, D., Mosbrugger, V., Zhang, R., Xu, B., Dozier, J., Gillespie, T., Gu, Y., Kang, S., Piao, S., Sugimoto, S., Ueno, K., Wang, L., Wang, W., Zhang, F., Sheng, Y., Guo, W.,

https://doi.org/10.5194/egusphere-2025-2187
Preprint. Discussion started: 17 June 2025

Ailikun, Yang, X., Ma, Y., Shen, S. S. P., Su, Z., Chen, F., Liang, S., Liu, Y., Singh, V. P., Yang, K., Yang, D., Zhao, X., Qian, Y., Zhang, Y., and Li, Q.: Recent Third Pole's Rapid Warming Accompanies Cryospheric Melt and Water Cycle Intensification and Interactions between Monsoon and Environment: Multidisciplinary Approach with Observations, Modeling, and Analysis, Bulletin of the American Meteorological Society, 100, 423–444, https://doi.org/10.1175/BAMS-D-17-0057.1, 2019.

Yi, Y., Wu, T., Wu, M., Jiang, H., Yang, Y., and Rogers, B. M.: Abrupt thaw and its effects on permafrost carbon emissions in the Tibetan Plateau: A remote sensing and modeling perspective, Earth-Science Reviews, 261, 105 020, https://doi.org/10.1016/j.earscirev.2024.105020, 2025.

Young, J. M., Farquharson, L. M., Luo, J., Nesterova, N., Van Der Sluijs, J., and Kokelj, S. V.: Permafrost mass wasting in ice-rich landscapes: recent advances (2013 to 2024) on mechanisms, dynamics, and impacts, in review.

Zhao, L., Zou, D., Hu, G., Du, E., Pang, Q., Xiao, Y., Li, R., Sheng, Y., Wu, X., Sun, Z., Wang, L., Wang, C., Ma, L., Zhou, H., and Liu, S.: Changing climate and the permafrost environment on the Qinghai–Tibet (Xizang) plateau, Permafrost and Periglacial Processes, 31, 396–405, https://doi.org/10.1002/ppp.2056, 2020.

Zhao, L., Zou, D., Hu, G., Wu, T., Du, E., Liu, G., Xiao, Y., Li, R., Pang, Q., Qiao, Y., Wu, X., Sun, Z., Xing, Z., Sheng, Y., Zhao, Y., Shi, J., Xie, C., Wang, L., Wang, C., and Cheng, G.: A synthesis dataset of permafrost thermal state for the Qinghai–Tibet (Xizang) Plateau, China, Earth System Science Data, 13, 4207–4218, https://doi.org/10.5194/essd-13-4207-2021, 2021.

Zou, D., Zhao, L., Sheng, Y., Chen, J., Hu, G., Wu, T., Wu, J., Xie, C., Wu, X., Pang, Q., Wang, W., Du, E., Li, W., Liu, G., Li, J., Qin, Y., Qiao, Y., Wang, Z., Shi, J., and Cheng, G.: A new map of permafrost distribution on the Tibetan Plateau, The Cryosphere, 11, 2527–2542, https://doi.org/10.5194/tc-11-2527-2017, 2017.

Zou, D., Pang, Q., Zhao, L., Wang, L., Hu, G., Du, E., Liu, G., Liu, S., and Liu, Y.: Estimation of Permafrost Ground Ice to 10 m Depth on the Qinghai-Tibet Plateau, Permafrost and Periglacial Processes, p. ppp.2226, https://doi.org/10.1002/ppp.2226, 2024.